Aalto University School of Electrical Engineering
Department of Signal Processing and Acoustics
Metrology Research Institute

Miikka Kivi

# Sample Alignment for Diffuse Reflectance Measurements

Thesis submitted in fulfilment of the requirements for the degree of Master of Science in Technology.

Espoo, 19.11.2014

Thesis supervisor: Prof. Erkki Ikonen

Thesis instructor: M.Sc. Priit Jaanson

**Author:** Miikka Kivi

**Name of the Thesis:** Sample Alignment for Diffuse Reflectance Measurements

**School:** Electrical Engineering

**Department:** Signal Processing and Acoustics

**Professorship:** S-108 Measurement Science and Technology

**Date:** 19.11.2014 **Number of pages:** 43

**Supervisor:** Prof. Erkki Ikonen

**Instructor:** M.Sc. Priit Jaanson

Accurate measurements of material reflectance rely heavily on the accurate placement and alignment of the sample. Majority of currently existing sample alignment methods utilize an alignment laser in some way, but the roughness of diffusely reflecting surfaces prevent the use of such methods directly with that kind of sample, and a separate reflective piece must often be used. In this master's thesis, a new camera based sample alignment method designed for diffuse reflectance measurements is introduced.

The method described in this work consists of a set of procedures for detecting the sample's linear and angular displacement from a reference point in the goniometric system. The method relies on detection of rigid features in the scene. Sample edges are observed to detect rotational angle of the sample, and sample holder corners are observed to calculate the center of rotation.

The performance of this method is studied in an effort to learn about the various sources of error. Cases that were studied include scene lighting conditions and reliability of the different parts of the detection algorithm. The testing was done on modest equipment and an overall accuracy of 230µm for center localization and 0.01° for rotational angle was achieved. The system is, however, inherently limited by the physical characteristics of the camera, as well as the size and distance to the sample. On the other hand, this also means that the alignment method is versatile and scalable, as the details of the detection algorithm can be modified to meet the requirements of a given project, and higher quality cameras can be purchased.

**Keywords:** Sample alignment, diffuse reflectance, reflectance measurement, machine vision, camera, edge detection, Hough transform, center of rotation, perspective, feature detection.

**Tekijä:** Miikka Kivi

**Diplomityön nimi:** Näytteen suuntaus hajaheijastusmittauksissa

**Koulu:** Sähkötekniikan korkeakoulu

**Osasto:** Signaalinkäsittely ja akustiikka

**Professuuri:** S-108 Mittaustekniikka

**Päivämäärä:** 19.11.2014 **Sivumäärä:** 43

**Valvoja:** Prof. Erkki Ikonen

**Ohjaaja:** DI. Priit Jaanson

Materiaalien tarkat heijastusmittaukset edellyttävät näytteen täsmällistä sijoittamista ja suuntaamista. Valtaosa tämänhetkisistä suuntausmenetelmistä käyttää jollain tavalla hyväksi suuntauslaseria, mutta hajaheijastavien pintojen karheus estää tällaisten menetelmien käytön suoraan kyseisen tyyppisestä näytteestä. Tällöin on usein käytettävä erillistä heijastavaa suuntauskappaletta. Tässä diplomityössä esitellään uusi, kameroihin perustuva näytteensuuntausmenetelmä, joka on suunniteltu käytettäväksi hajaheijastusmittauksissa.

Tässä työssä esitelty menetelmä koostuu sarjasta prosesseja, joilla havaitaan näytteen lineaari- ja kulmapoikkeama referenssipisteestä goniometrisessä systeemissä. Menetelmä pohjautuu kuvassa olevien selkeiden piirteiden havaitsemiseen. Näytteen reunoja käytetään näytteen rotaatiokulman havaitsemiseen, ja näytteen pidikkeen kulmia käytetään pyörimisen keskipisteen laskemiseen.

Uuden menetelmän suorituskykyä tutkittiin siihen vaikuttavia virhelähteitä etsimällä. Tutkittuja kohteita olivat valaistusolosuhteet, sekä menetelmän eri osien luotettavuus. Mittaukset tehtiin vaatimattomilla laitteilla, joilla kokonaistarkkuudeksi saatiin 230 µm pyörimisen keskipisteelle, sekä 0,01° rotaatiokulmalle. Menetelmää rajoittaa kuitenkin aina kameran fyysisten ominaisuuksien lisäksi myös näytteen koko sekä etäisyys kamerasta. Toisaalta tämä tarkoittaa myös, että menetelmä on monikäyttöinen ja skaalautuva, sillä algoritmin yksityiskohtia voidaan muokata kullekin projektille sopivaksi, ja korkeampilaatuisia kameroita voidaan ostaa.

**Avainsanat:** Näytteen suuntaus, hajaheijastus, heijastusmittaukset, konenäkö, kamera, reunantunnistus, Hough-muunnos, pyörimisen keskipiste, perspektiivi, ominaisuuden havaitseminen

# Table of Contents

# Forewords

This master's thesis has been made at the Department of Signal Processing and Acoustics at Aalto University. I am forever thankful to Professor Erkki Ikonen for this opportunity, and for the trust that I've received while working on my thesis.

The subject of this work presented an interesting problem for me to solve. I am thankful for all the help and guidance I've received not only from my instructor, Priit Jaanson, but also from Farshid Manoocheri. Their contributions to this work have been invaluable. I would also like to extend my gratitude to all my colleagues at Metrology research group, who have made this workplace a pleasant and memorable experience.

This work is the culmination of years of studying, and there is more one person who deserves recognition. For twelve years she has been nothing but a positive force in my life. I dedicate this work to the mother of my unborn child, Nina Barman.

Espoo, 19.11.2014

Miikka Kivi

# Symbols and terms

| | |
|---|---|
| $\theta$ | Zenith angle |
| $\varphi$ | Polar angle |
| $\omega_{i,}$ $\omega_r$ | Directions of radiation |
| $\rho$ | Radius in a polar coordinate system |
| $\beta_a$, $\beta_b$ | Auxiliary variable used in eccentricity error calculations |
| *BRDF* | Bidirectional reflectance distribution function |
| *E* | Irradiance |
| *fps* | Frames per second, the unit of video frame rate |
| $f_r$ | Bidirectional reflectance distribution function |
| *h* | Camera distance from a sample |
| *R* | Radius of a of a circle |
| $k_e$, $k_c$ | Slopes of ellipse and circle normal, respectively |
| $k_{cl}$ | Slope of a line connecting two points of a circle |
| $k_{pb}$ | Slope of a perpendicular bisector |
| *L* | Radiance |
| *T1, T2* | Threshold values used in filtering algorithm |
| $x_i$, $x_j$, $y_i$, $y_j$ | Coordinates for points in a recorded path of a corner |
| $x_{ij}$, $y_{ij}$ | Coordinates for middle point of a line connecting two points in a path |
| $x_{int}$, $y_{int}$ | Coordinates for bisector intersection location |

*Gonioreflectometer* is a device used to measure the bidirectional reflectance distribution function of a surface.

*Perpendicular bisector* is a line which divides segment of another line in half, and is perpendicular to that segment.

*Slope* is the value which determines the direction and steepness of a line.

# 1. Introduction

Diffuse reflectance measurements provide valuable information on material properties for use in various industrial and research applications. These measurements are typically performed relative to a reference standard that is traceable to an absolute scale. Several methods for realizing the absolute scale exist, and while majority of them are based on an integrating sphere method, a gonioreflometric approach was chosen due to its versatility when an absolute scale was realized at Aalto University [1]. In this type of setup, there are two rotating parts that need to be aligned concentrically. Previously the alignment of the sample holder was performed by illuminating a dummy sample with an alignment laser. The sample holder would then be rotated, and if the illuminated spot would move in relation to a reference point on the dummy sample surface, the positioning of the sample holder would need to be adjusted and process was repeated until alignment was deemed sufficient. This method could not be applied directly with a proper sample, since relative displacement of the illuminated spot could not be reliably resolved without discernible features on the sample surface, such as crosshair markings. The alignment of the rotating cantilever was done similarly, by examining how the reflected laser beam would reach the detector, and adjusting the alignment until satisfactory performance was reached.

A camera based sample alignment method is described in this paper. In the following chapters, current diffuse reflectance measurement setups will be introduced, as well as my solution to improving their sample alignment process. The issues that affect the uncertainty of this new method will be studied and discussed. Main advantages of this alignment method include the ability to confirm manual alignment adjustments with a PC, the ease of alignment process and the ability to utilize the method in various different measurement conditions.

## 1.1. Diffuse reflectance measurements

Today's computer graphics place a tremendous emphasis on visual realism, and one of the major challenges of that is accurate measurements and modelling of light scattering [2]. The scattered light from a surface is usually described by a bidirectional reflectance distribution function (BRDF); a four-dimensional function describing how light incident on a surface is distributed over the hemisphere above when reflected. It is defined in equation (1.1), and illustrated in Figure 1

$$f_r(\omega_i, \omega_r) = \frac{dL_r(\omega_r)}{dE_i(\omega_i)} = \frac{dL_r(\omega_r)}{L_i(\omega_i)\cos(\theta_i)\, d\omega_i}, \tag{1.1}$$

where $L_i$ and $L_r$ are radiances, and $E_i$ is irradiance. Indices $i$ and $r$ indicate incident and reflected light, respectively. The four-dimensionality comes from the fact that directions $\omega_i$ and $\omega_r$ are both parameterized by their polar angle $\varphi$, and zenith angle $\theta$.

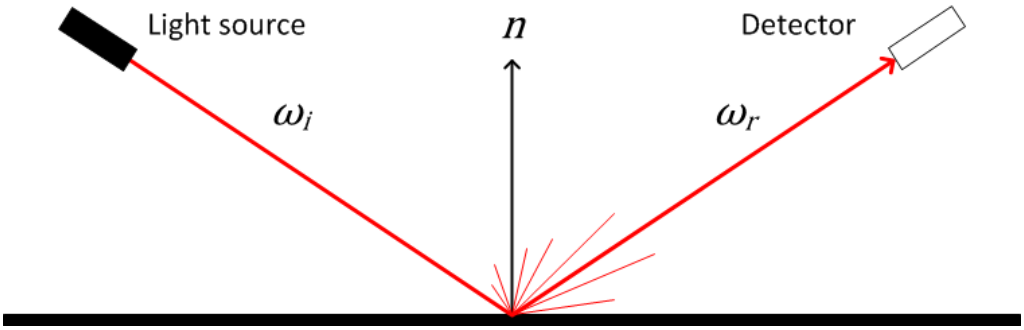


**Figure 1: Geometry of bidirectional reflectance distribution function.**

Since BRDF is a four-dimensional function, a two-axis goniometer and vast amount of time are required for direct measurements over both polar and zenith angles. In many cases, multiple-axis robot is utilized instead, as was done in Physikalisch-Technische Bundesanstalt [3]. However, in the case of 0° incidence zenith angle, direct measurements over both reflected angles are not necessarily required, as cylindrical symmetry can be assumed for high-quality samples [1], and the complexity of the measurement setup can be greatly reduced by performing the measurement over detector zenith angles only.

Gonioreflectometer is a device for measuring the BRDF from a sample. It consists of a light source capable of illuminating the sample, and a sensor for detecting the reflected light around the sample. The word gonio in the name comes from a Greek word meaning angle. A schematic of the gonioreflectometer setup used at Aalto University is shown in Figure 2. The incident light is guided through a double monochromator and a set of guiding mirrors. The sample surface is placed at the center of a turntable where the sample and the detector can be rotated coaxially.

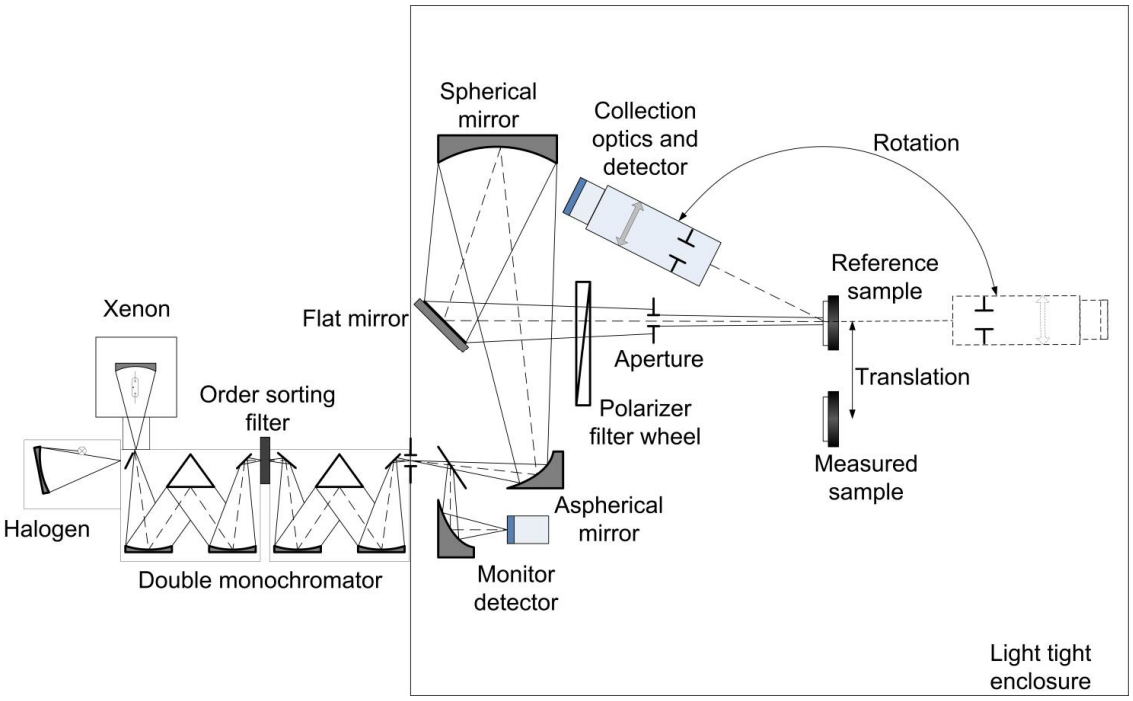


**Figure 2: Schematic of the gonioreflectometer setup.**

## 1.2. **Sample alignment**

In the gonioreflectometer setup, the sample is placed at the center of a turntable. If the sample is misaligned, the true angle between incident and reflected light will differ from intended angle as shown in Figure 3.

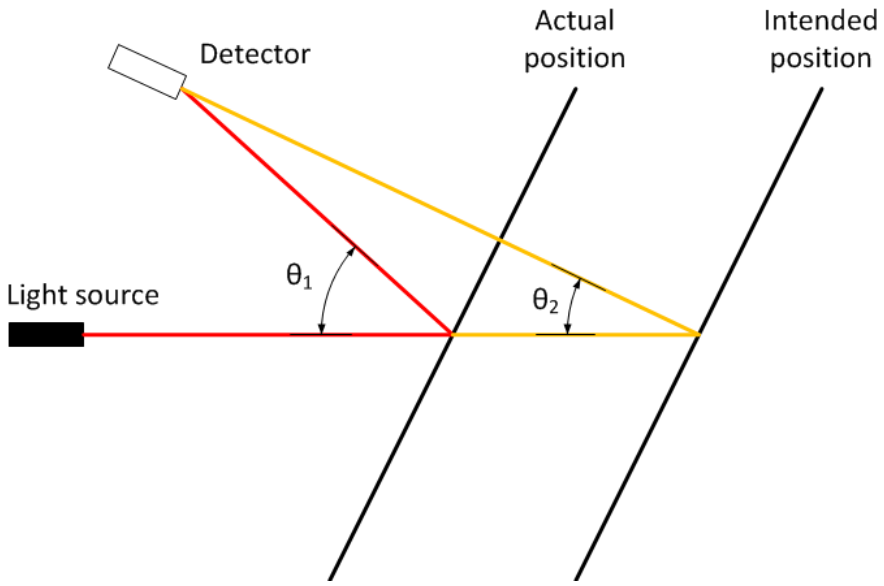


**Figure 3: Sample misalignment affects the geometry of measured BRDF.**

Errors will also occur if there is angular misalignment of the sample. The angular alignment was previously handled by illuminating a dummy sample surface at normal incidence, and observing the position of the illuminated spot relative to the sample center point. If the illuminated spot did not move when the sample was rotated, then proper alignment was achieved. On the other hand, if the illuminated spot did move, then it meant that the center of rotation did not lie on the intersection of the sample surface and incident light. Observing the relative displacement of the illuminated spot illustrated in Figure 4, it is possible to calculate where the center of rotation lies relative to the surface, and adjust the setup accordingly.

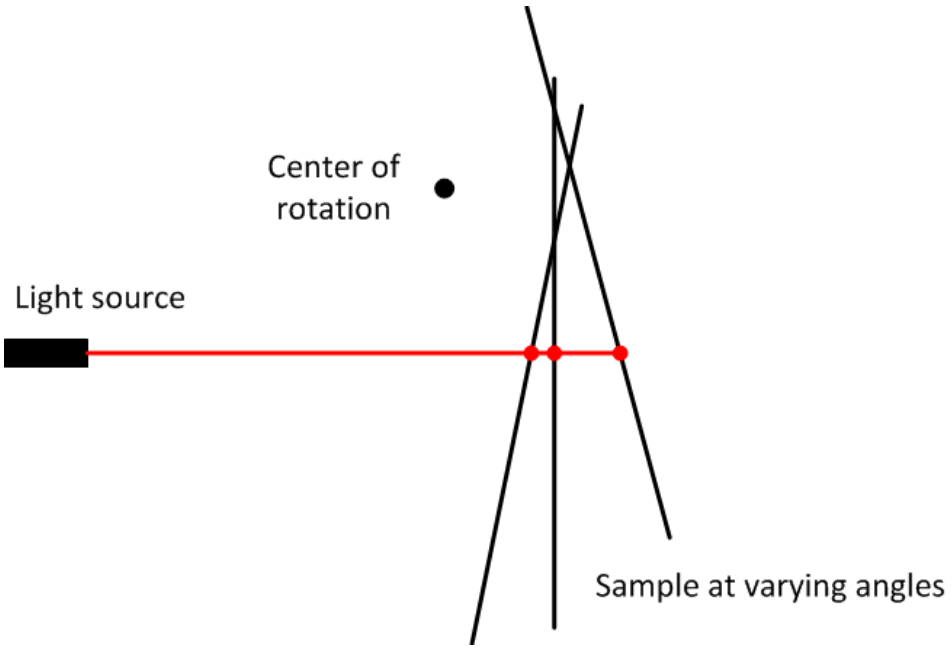


**Figure 4: Relative position of the illuminated spot on the sample surface changes when misaligned sample is rotated.**

However, this method is fairly cumbersome, and it can only be done on a dummy sample, since relative position of the illuminated spot is very difficult to measure from a sample without discernible features, such as crosshair markings. For reflective surfaces, the reflected beam could be detected and the geometry of the setup could easily be resolved, but a fundamental property of a diffusely reflecting surface is, that the light scatters, rendering this option unusable. In the following chapters, a camera based alignment system designed directly for diffusely reflecting samples is introduced.

## 1.3. **Existing alignment methods**

### 1.3.1. xDReflect

A joint research project “Multidimensional reflectometry for industry”, also known as xDReflect, describes one technique for sample alignment [4]. Their method is as follows. Four alignment posts are placed exactly at positions 45, 135, 225 and 315 degrees in relation to principal axis. These posts have holes drilled through them, so that when two lasers are positioned according to Figure 5, their beams go through the alignment posts and cross at the center of the turntable. Next, a robot arm is used to position a reflective surface on the position where the beams cross. The rotation of the sample is adjusted so that the light from one laser passes through holes in alignment posts placed at 45 and 315 degrees. The alignment is then complete, and the robot arm origin is set at that position.

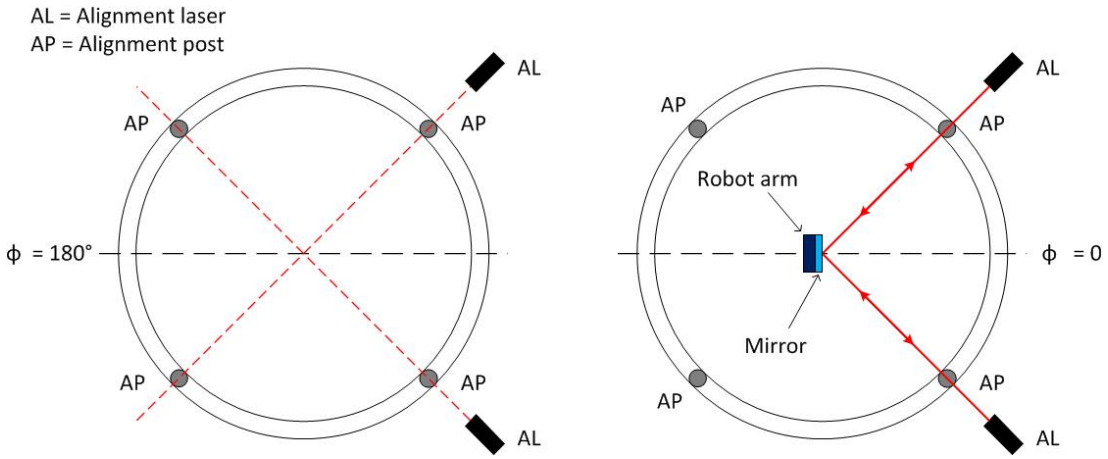


**Figure 5: xDReflect's implementation of alignment procedure.**

There are several issues with this implementation. Firstly, it requires the use of a turntable with very accurately placed mounting positions for alignment posts. In essence, the alignment of the alignment posts has to be already known to be accurate. Secondly, since the alignment is done using lasers, the surface held by robot arm at the center has to be reflective. Light reflected from diffuse surfaces will scatter, and for such measurements the actual sample must be placed in the system after it has been aligned. It is possible that the alignment shifts in the process of switching the sample.

### 1.3.2. 3D scanning

Commercially available products for 3D scanning are available from various companies. Figure 6 shows an ATOS device by the company “GOM mbH - Gesellschaft für Optische Messtechnik”. This type of device has a projector which illuminates the sample with structured light; a known pattern, usually made of lines or grids. Two or more cameras then detect the apparent distortion to the pattern, which is used to generate a reconstruction of the scene.

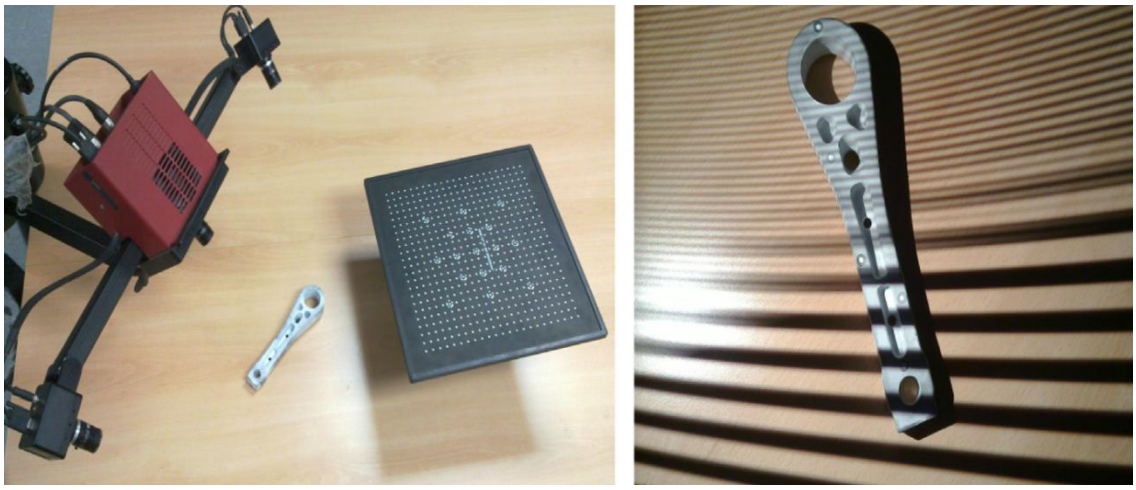

**Figure 6: 3D scanning device [5].**

This type of devices have proven to be very precise and have high repeatability, although the accuracy remains unknown since the algorithms used have not been made public by the companies that manufacture the devices [6]. While a 3D scanner can be an effective tool for resolving sample displacement relative to the scanner, utilizing one in a gonioreflectometer would require the position of the scanner itself to be known accurately. For most applications though, the most limiting factor is likely the price of the scanner, which can be in the order of tens of thousands of euros for high quality devices.

## 1.4. **Planned alignment method**

The idea is to use two cameras to resolve the displacement and alignment of the sample. A camera placed on the side of the sample is used to resolve the angle between the sample surface and a vertical reference pole. Placement of the side camera does not need to be accurate; it only requires simultaneous view of the sample and the reference pole. Another camera is placed directly on top of the system, at the rotational axis of the turntables. Accurate placement of the top camera is more important than it is for the side camera, and this can be achieved by observing the apparent eccentricity of the turntable. This is discussed in greater detail in section 3.4. Like the side camera, the top camera is used for resolving rotational displacement of the sample, but it is also used to detect the position of the sample. The proposed detection algorithm is introduced in section 3.3. Additionally, the top camera can be used to determine the concentricity of the turntables. Schematic of the planned setup is shown in Figure 7.

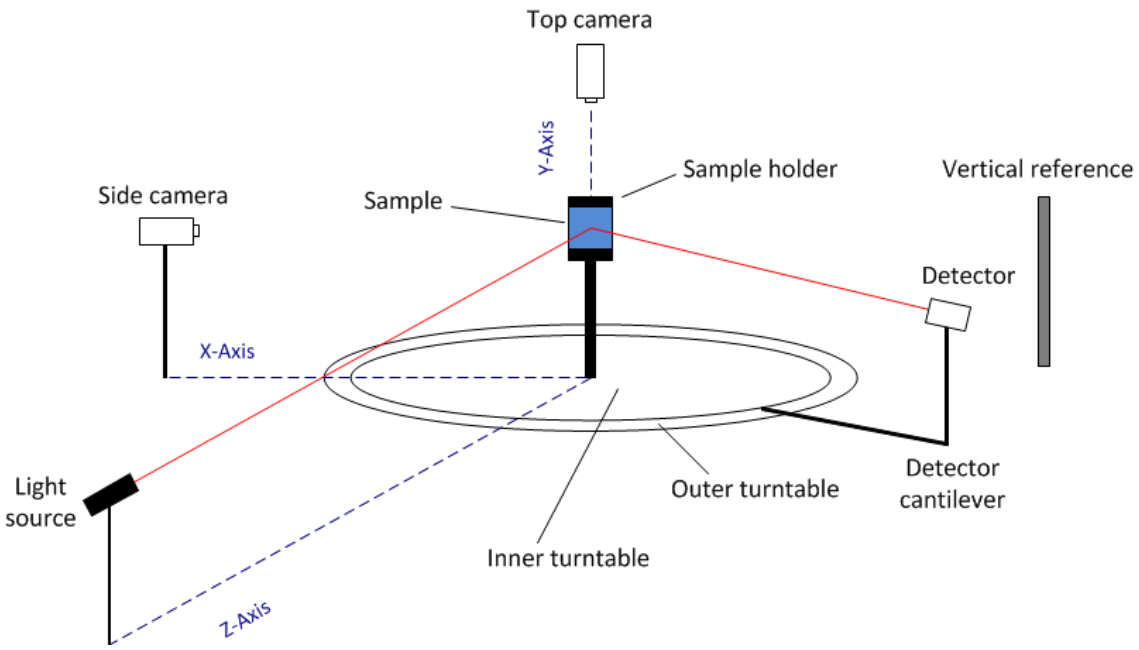


**Figure 7: Schematic of the planned alignment method.**

# 2. Principles of camera based feature detection

We know from nature that vision based sensory is a powerful tool; the evolution of the eye has occurred multiple times independent of one another. Even so, it is the brain that ultimately decodes the sensory information and decides which part of it is important. Machine vision and feature detection mimics biological vision very closely, and similarly the quality of the machine vision system is dependent on the characteristics of the camera as well as the efficiency of the detection algorithm.

## 2.1. **Edge detection**

The basic principle of edge detection is fairly simple. Each pixel in an image is reduced to a number value, typically corresponding to its brightness. An edge is then detectable as the region in an image, where this value changes sharply. Identifying this region is achieved by convolving the image with a filtering mask, which is designed in a way that produces zero output at uniform areas, and high output where there is edge present. Shown on Figure 8, each pixel value is multiplied with a coefficient from a corresponding slot in the filter, and added together to form final matrix.

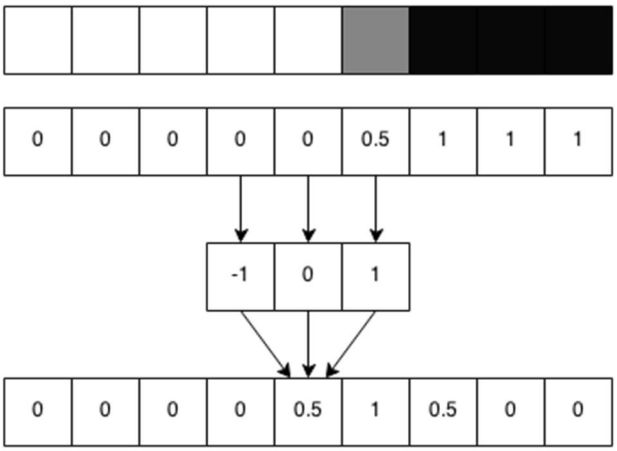


**Figure 8: Basic principle of filtering mask used in edge detection.**

There are a large number of different masks that can be used; each designed to be sensitive to different types of edges. These differences include properties such as edge orientation, sharpness and image noise level [7]. A comparison of several commonly used masks is shown in Figure 9.

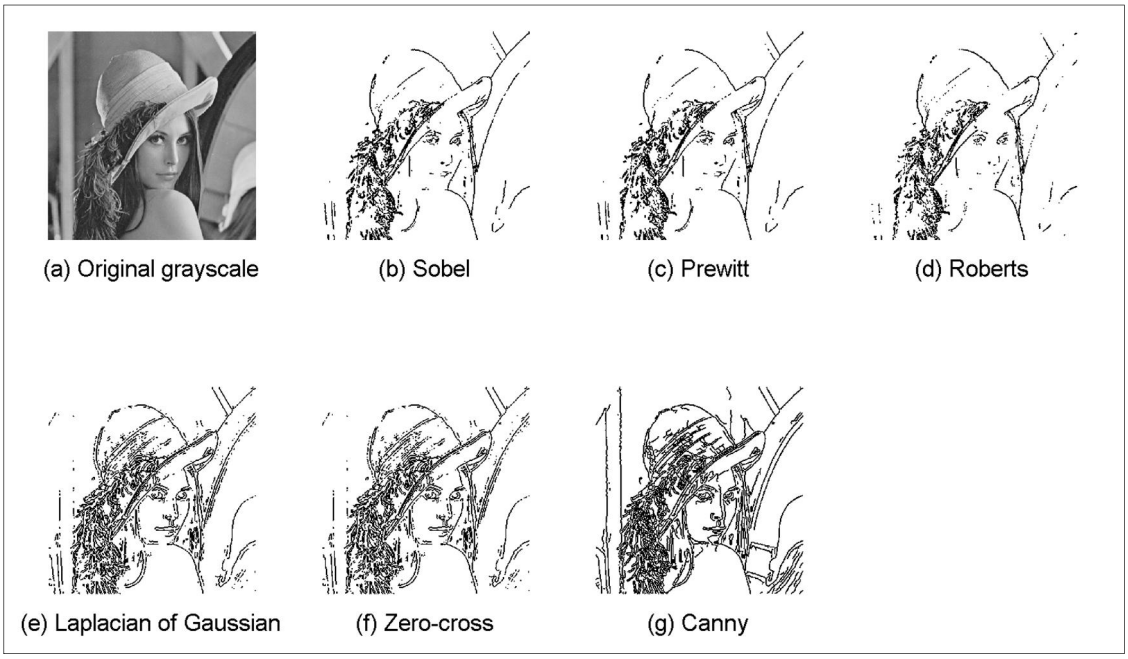


**Figure 9: Comparison of edge detection methods.**

In 1986, John Canny set out to improve existing edge detection methods. His primary criteria were to reduce error rate, improve spatial accuracy of edges, and prevent multiple responses to a single edge [8]. His work proved to be very successful, and his method is still widely regarded as the best option for majority of applications.

## 2.2. **Hough transform**

Simple edge detection algorithms only produce set of points with no extra information, such as how those points are connected to each other. We want to discover straight lines, which we can use to determine sample properties such as alignment. Hough transform is a powerful method for automatically defining straight lines in an image [9]. A set of lines passing through a single point in XY-coordinate system is typically formulated as in equation (2.1)

$$y_i = mx_i + c. \tag{2.1}$$

If we simply move the terms around to obtain equation (2.2)

$$c = -x_i m + y_i, \tag{2.2}$$

it becomes apparent that this set of points represents a line in MC-coordinate system, as seen in Figure 10.

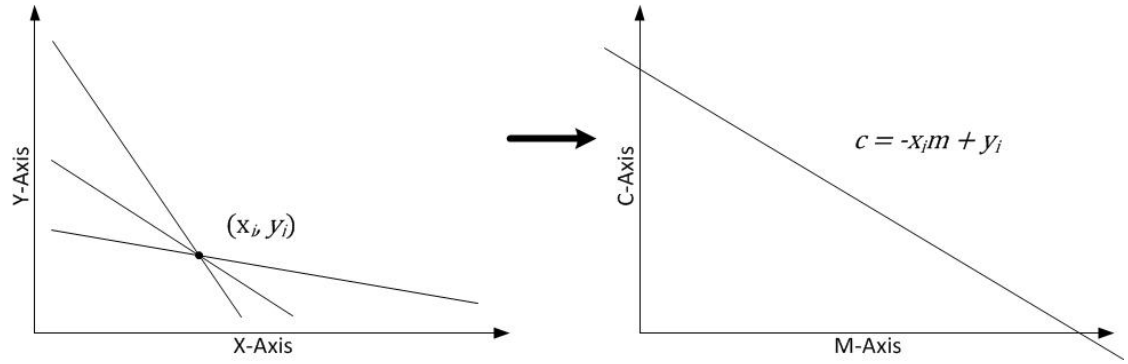


**Figure 10: A set of lines passing through a point in the XY-coordinate system transforms into a line in the MC-coordinate system.**

In other words, every point of a line in (M, C) represents a single line in (X, Y). If we now consider a line *L* passing through two points in the XY-coordinate system, then that line must lie on an intersection of two lines in the MC-coordinate system as seen in Figure 11:

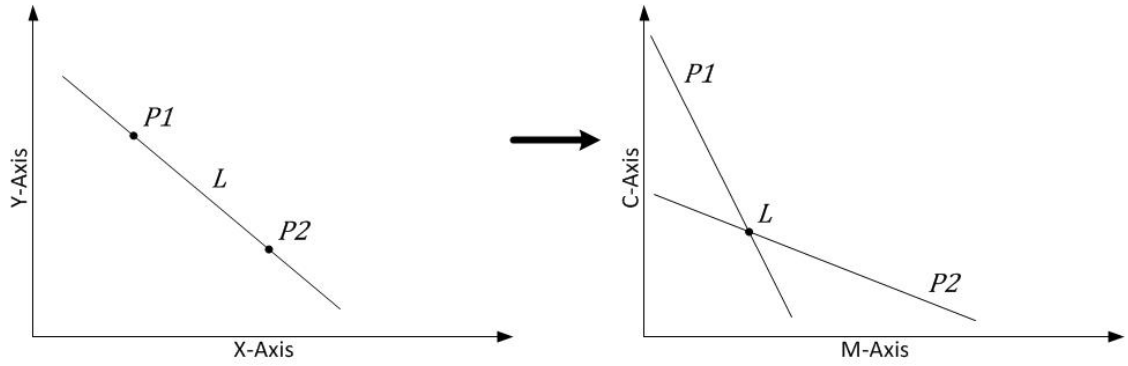


**Figure 11: Single line in XY-coordinate system transforms into a point in MC-coordinate system.**

In practice, the MC-coordinate system is rarely used, since any vertical line would entail the value at *m* in equation (2.2) to become infinite. Instead, a line is typically defined by its (ρ, θ) coordinates, as seen in Figure 12, and defined in equation (2.3),

$$x\cos(\theta) + y\sin(\theta) = \rho. \qquad (2.3)$$

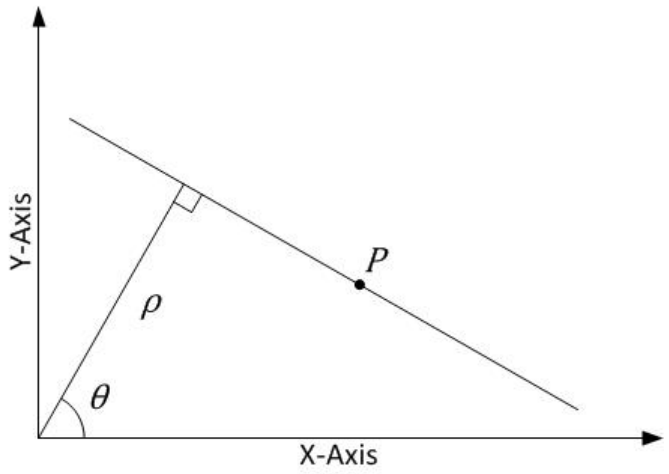


**Figure 12: A line in the XY-coordinate system defined by (ρ, θ).**

This means that a point in (X, Y) is not transformed into a line in (M, C), but a curve in (ρ, θ). The process still remains the same, and similarly to Figure 11, a specific line in (X, Y) can be found from an intersection of curves in (ρ, θ), as seen in Figure 13.

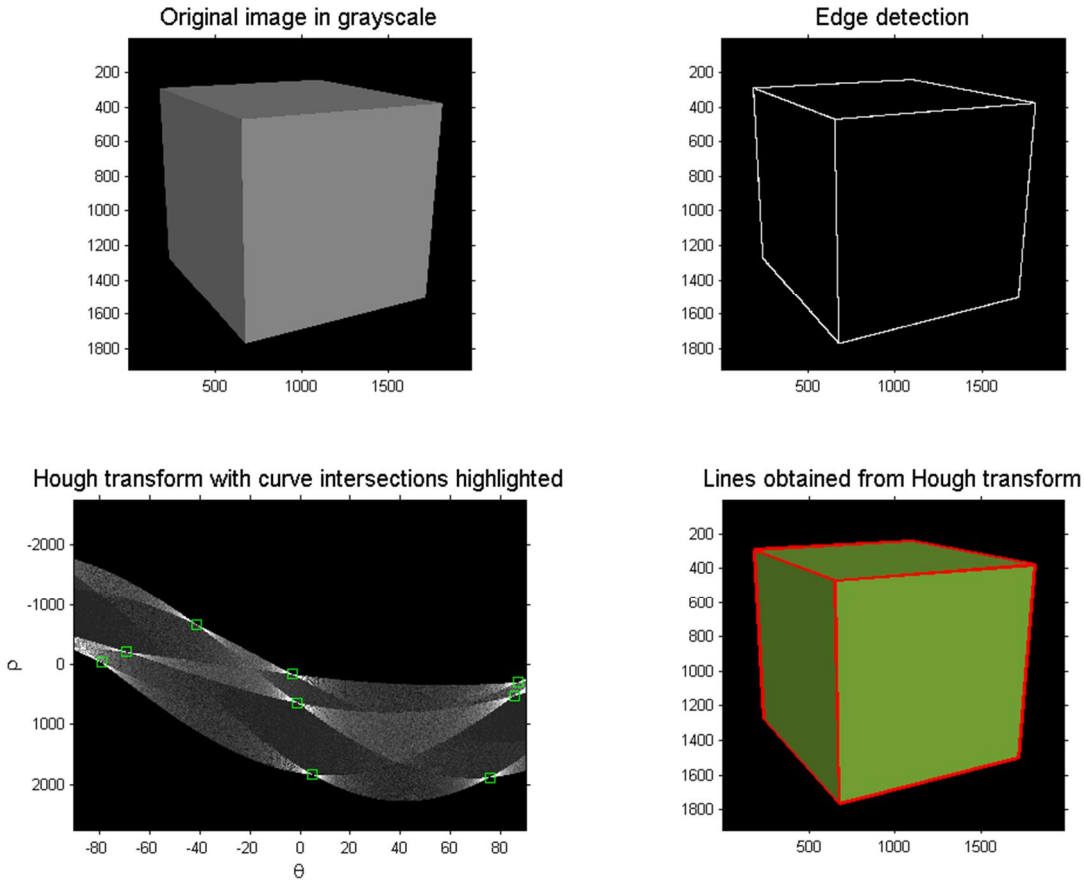


**Figure 13: Finding straight lines from an image using Hough transform.**

The goal is to utilize straight line detection as a method of resolving sample alignment in the measurement setup. The angle of detected line is presented in the computer as can be seen from an example in Figure 14, and the information of current orientation can then be used by the operator to properly align the sample.

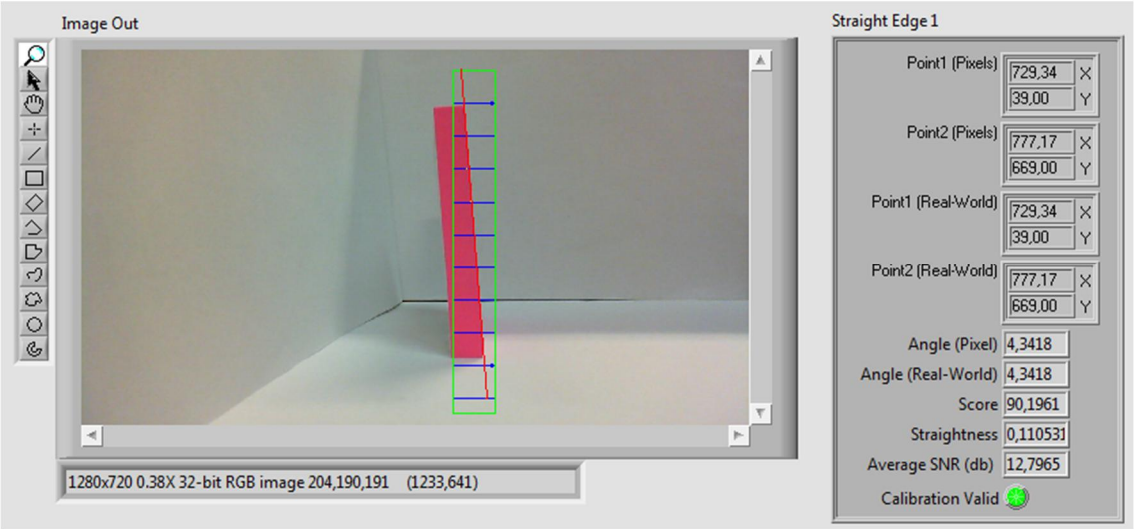


**Figure 14: Camera used to resolve the angular alignment of an object.**

The total amount of information contained on a video is huge, and because the program runs in real-time, there is a time constraint on the edge detection algorithm. This is why edge detection algorithms are rarely applied on the entire image. In the program used in this work, the edges are only detected from limited amount of lines, shown in blue, in a selected region of the image, shown in green, in Figure 14.

# 3. Measurement setup

During gonioreflectometric measurements, the sample will be placed on a turntable and will be rotated in synchronization with the detector. If the sample location is misaligned, the distances between light source, sample and detector will vary as the table is turned. We want to find out what is the center of rotation when the table is turned, and align the sample so that the center of rotation lies exactly at the sample surface plane. The operating principle is shown in Figure 15, which shows that if the center of rotation is fixed, then all points will rotate around it in a perfect circle and the center can be found by tracking image features, such as corners.

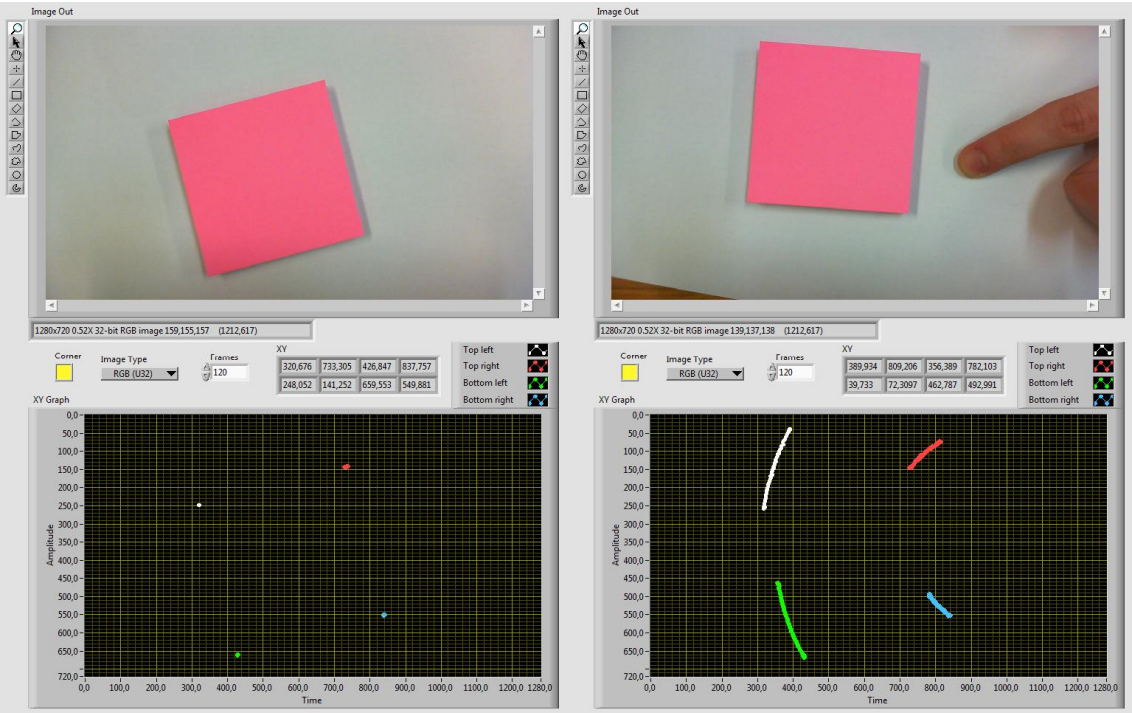


**Figure 15: Sample feature tracking reveals center of rotation.**

A prototype system shown in Figure 16 was built to study the feasibility of the alignment process. To easily position and align the sample holder, it was connected to a system connecting a turntable, a linear translator, and a three-axis platform. Together they form a system where the sample holder could be adjusted with 5 degrees of freedom. The two cameras used to examine the sample were placed over the sample and to the side of the sample. An array of 4 LED light sources was also used, as well as a diffuser not shown in the figure.

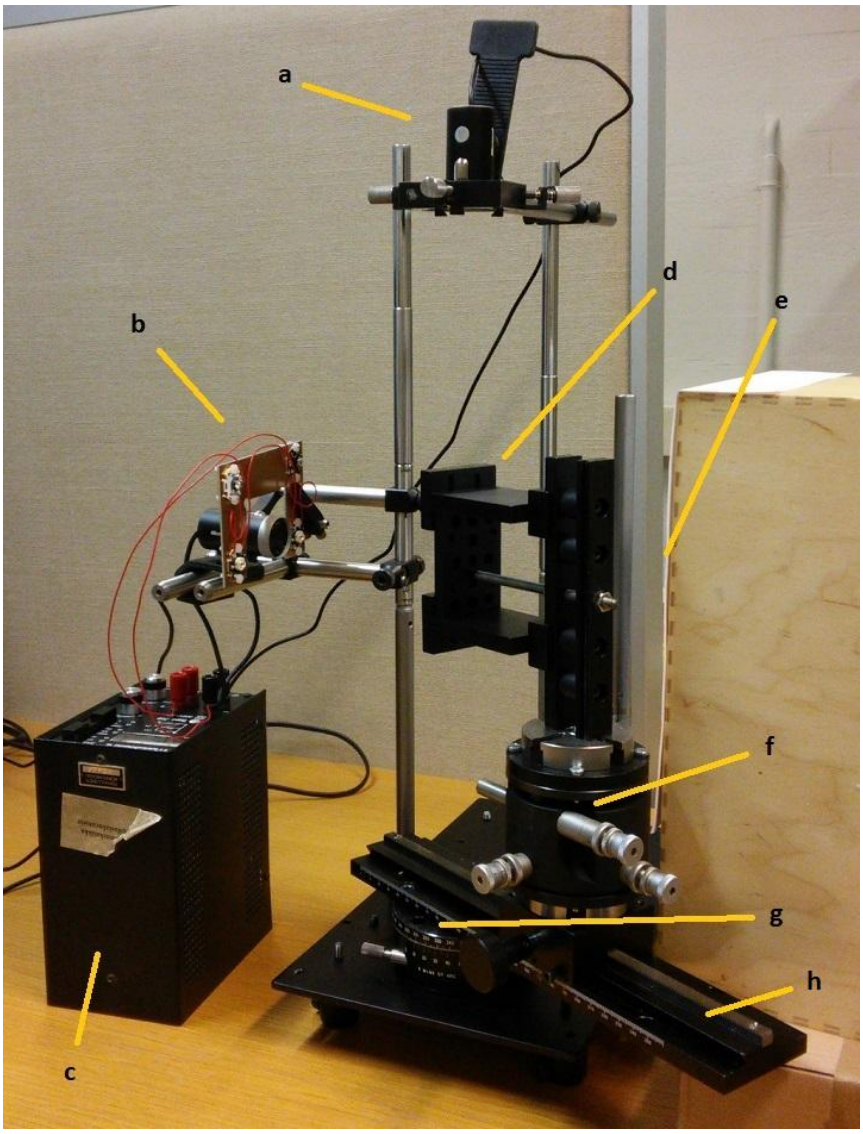


**Figure 16: Measurement setup. Marked parts are top camera (a), side camera with LED light sources (b), power supply (c), sample holder (d), white background (e), three-axis platform (f), turntable (g), and a linear translator (h).**

## 3.1. **Lighting**

Cameras can never capture truly perfect image of world objects due to noise, reflections, shadows, lens distortion and uneven illumination. While huge amount of image processing methods exist, the best way to achieve better image clarity is to improve the physical conditions of the setup. One of the problems of edge detection is shadows, which can make it difficult to automatically detect object edges correctly as shown in Figure 17.

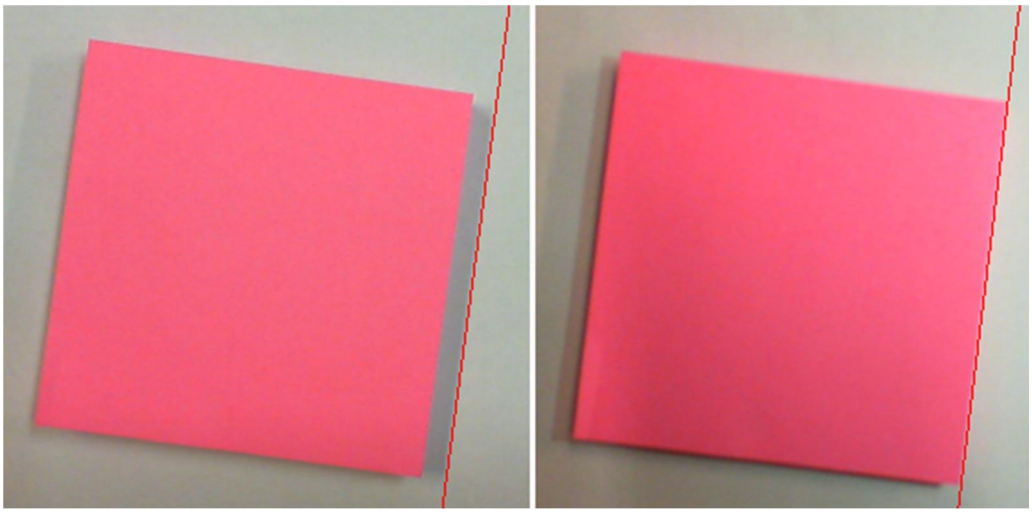

**Figure 17: Results of the same edge detection algorithm with different lighting conditions.**

Providing an even illumination on the sample is an effective way of getting rid of shadows. Using diffusers will increase the effective size of the light source, softening the shadows. A simple front lighting configuration shown in Figure 18(a) is sufficient for edge detection purposes, and was chosen for this work. Even greater shadow reduction could be achieved by positioning the light sources on the sides of the sample, and using reflected light from diffusers as seen in Figure 18(b) [10]. However, this configuration is slightly more complex to build, and it was not used in this work.

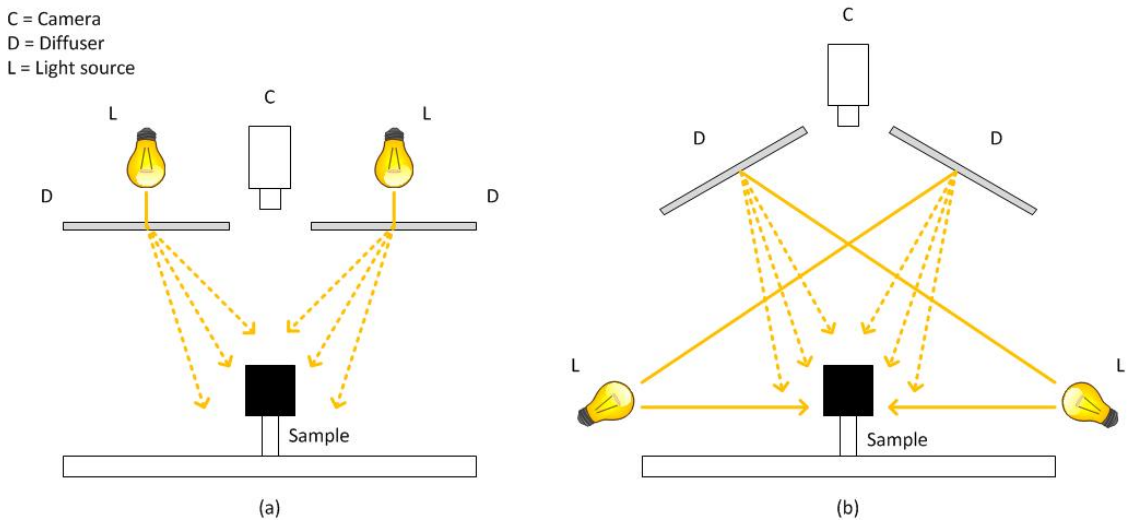


**Figure 18: (a) Diffuse front lighting. (b) Reflected diffuse front lighting.**

## 3.2. **Cameras**

Camera development over the past several years has lead up to a point where even the cheapest cameras can offer good accuracy in many machine vision applications. While such cameras are not the best performing cameras, their cheap price and ease of use led to the decision to use a pair of Microsoft LifeCam Cinema cameras (Part no. 6CH-00002) in the test setup. They feature OV9712 sensor by OmniVision, and provide a $M \times N$ = 1280×720 pixel resolution at 30 frames per second video. Spatial resolution $R_s$ of the camera is directly proportional to its 73° diagonal field of view $\alpha$, object distance $h$ and pixel resolution, according to equation (3.1),

$$R_s = \frac{2h \tan\left(\frac{1}{2}\alpha\right)}{\sqrt{M^2 + N^2}}. \tag{3.1}$$

For example, objects at 10 cm distance can be resolved at 100 µm/pixel accuracy.

## 3.3. **Center of rotation detection algorithm**

The principle behind finding the center of rotation lies in the symmetry that a perfect circle has. If you select any two points of a circle, draw a line that connects the two points, and finally draw a perpendicular bisector to that line, then the perpendicular bisector will always intersect with the center of the circle. The idea behind the algorithm is to record large amount of points in a circle, and then draw the connecting line and its perpendicular bisector for every possible point pair. The center of rotation can be found at the intersection of these bisectors, as illustrated in Figure 19. In the test setup, the sample holder is rotated on the turntable, and the top camera is set to track and record the path taken by the object corners. For each frame of video, there is a pixel coordinate address corresponding to their respective corners. In reality, each corner will rotate around the center point on a slightly different radius. However, this does not matter since all circles are concentric and the bisectors from all paths will intersect at the same position.

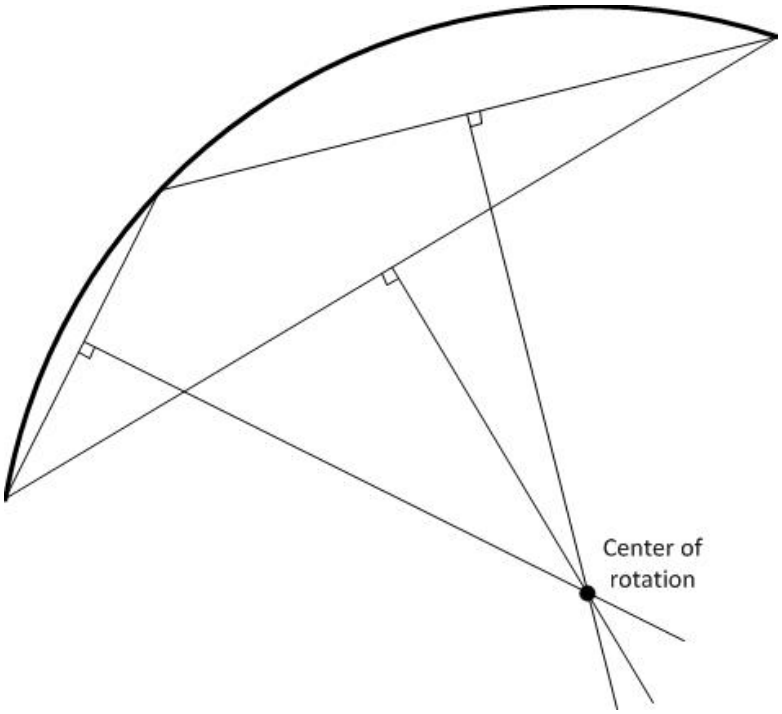


**Figure 19: Center of rotation is found at the intersection of perpendicular bisectors.**

We start by connecting each possible pixel pair in a given path. Center point of each connecting line is found from equation (3.2),

$$\begin{cases} x_{ij} = \frac{1}{2}(x_i + x_j) \\ y_{ij} = \frac{1}{2}(y_i + y_j). \end{cases} \tag{3.2}$$

The perpendicular bisector is a line intersecting that central point at a 90 degree angle. Its slope is therefore a negative inverse of the slope of the connecting line,

$$k_{pb} = -\frac{1}{k_{cl}} = \frac{x_i - x_j}{y_j - y_i}. \tag{3.3}$$

Using these values, all bisectors are fully parameterized in equation (3.4),

$$y - y_{ij} = k_{pb}(x - x_{ij}). \tag{3.4}$$

From the shape of the path seen on Figure 20, we can see that the bisectors to be drawn to this path should be roughly on a 45° angle, which corresponds to a slope value of around 0.5. As we calculate the bisector equations for every possible pixel pair in the

path, it becomes apparent that the recorded path is not an ideal arc of a circle. This is a problem especially for pixel pairs that are very close to each other, since the error in $k_{pb}$ can get extreme, as seen in Figure 21. However, the slope values are centered on the expected value of 0.5, and can therefore be considered accurate.

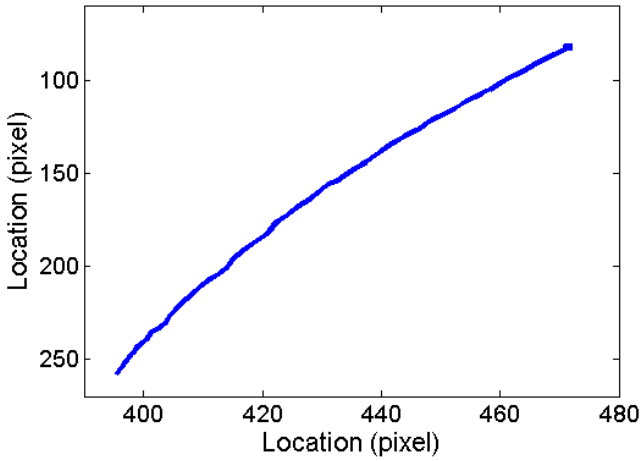


**Figure 20: Recorded corner path.**

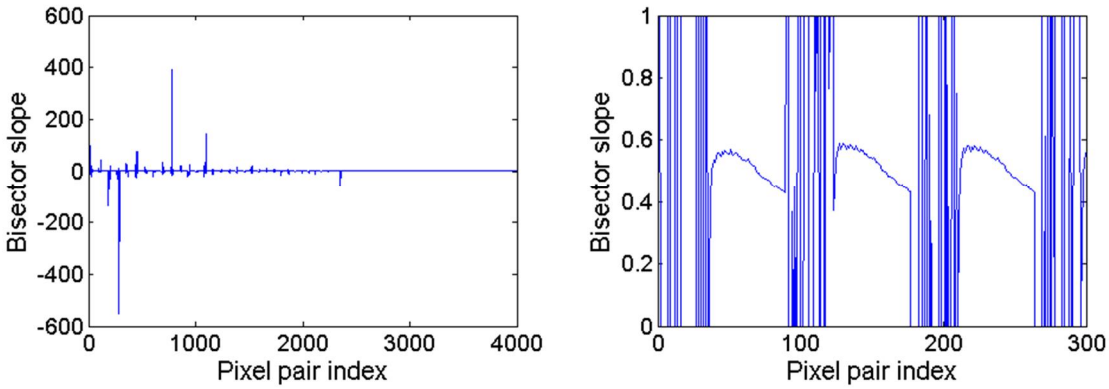


**Figure 21: Unfiltered bisector slope values.**

To get rid of the errors, we employ a two-stage filtering method. First, we set a threshold value that discards any data points with a slope value that differs from the median by more than chosen threshold value *T1*. This is done to discard large errors, which in turn enables us to better fit a curve into the data set. The data set is then thresholded against the fitted curve and again discarded if it differs from the fitted curve by chosen value *T2*. The effect of filtering is shown in Figure 22, in which each row illustrates a single corner, the left column is data after the first filtering phase and the right column after the second filtering phase. It is worth noting that the data acquired in this section was produced by moving the object by hand, and as such the data is very noisy.

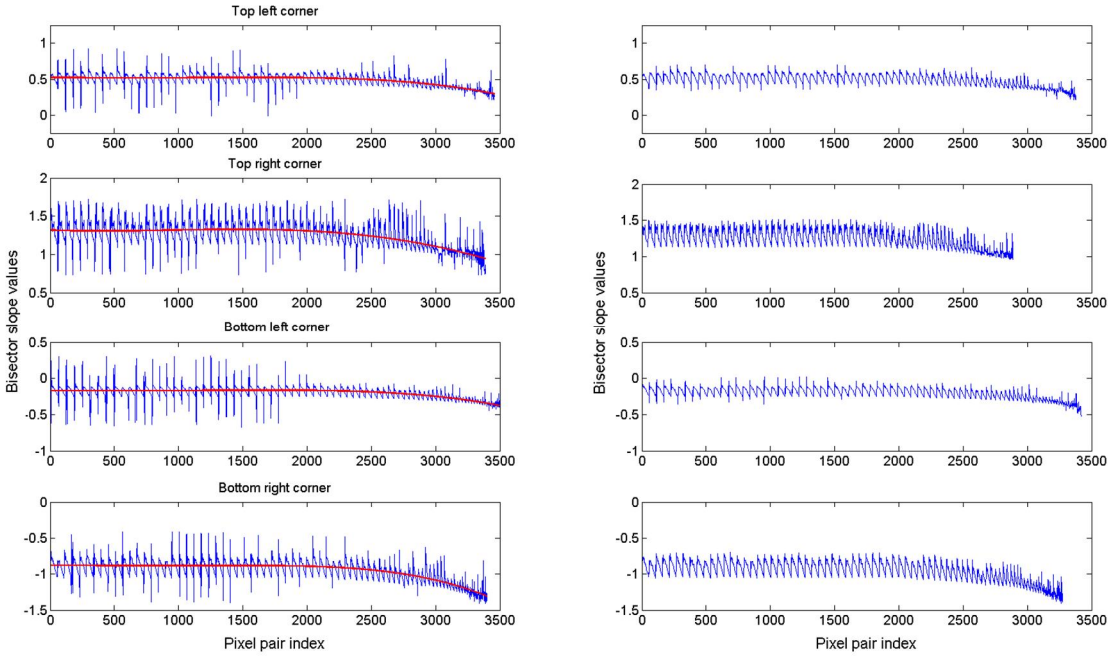


**Figure 22: Slope data. On the left a red curve is fitted into T1-filtered data, and on the right are shown data after T2-filtering.**

The fine structure in the shape of the filtered data is not random noise, but the result of the order in which the algorithm processes all the possible pixel pairs. The same is true for the overall downward bend in the last slope values. After filtering the data, the bisectors are drawn, and the center of rotation becomes apparent at the intersection of the bisectors shown in Figure 23.

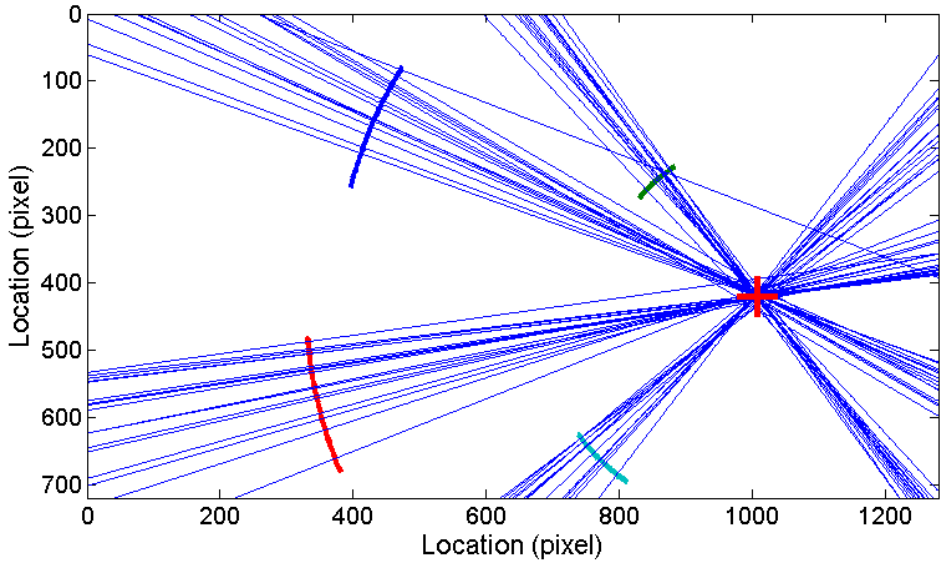


**Figure 23: Center of rotation is shown at the intersection of bisectors. Only every 200$^{th}$ line is drawn here.**

The center of rotation highlighted at Figure 23 is found by searching for a point which minimizes the lowest possible sum of distances to all intersection points,

$$D = \min_{x,y}\left(\sum_{int}\sqrt{(x - x_{int})^2 + (y - y_{int})^2}\right). \quad (3.5)$$

It is worth mentioning that the amount of bisector intersections can get quite high, and depending on the available hardware and software, the algorithm can get computationally intensive. With the example considered in this chapter, the corner movement was tracked over 90 frames which, after filtering, resulted in roughly 13 000 perpendicular bisectors and 84 000 000 intersection points. A computing time of several seconds is acceptable, since we don't need the calculations in real time. However, while calculations above were performed successfully in MATLAB, recreating the code in LabVIEW resulted in system running out of memory. It is therefore necessary to further disregard excessive bisectors. This is done by introducing percentage slider into the program pictured in Figure 24. This option randomly chooses a specified amount of bisectors, and uses them to calculate intersection points. This value should be chosen so that the number of intersections is as high as the computer is capable of calculating.

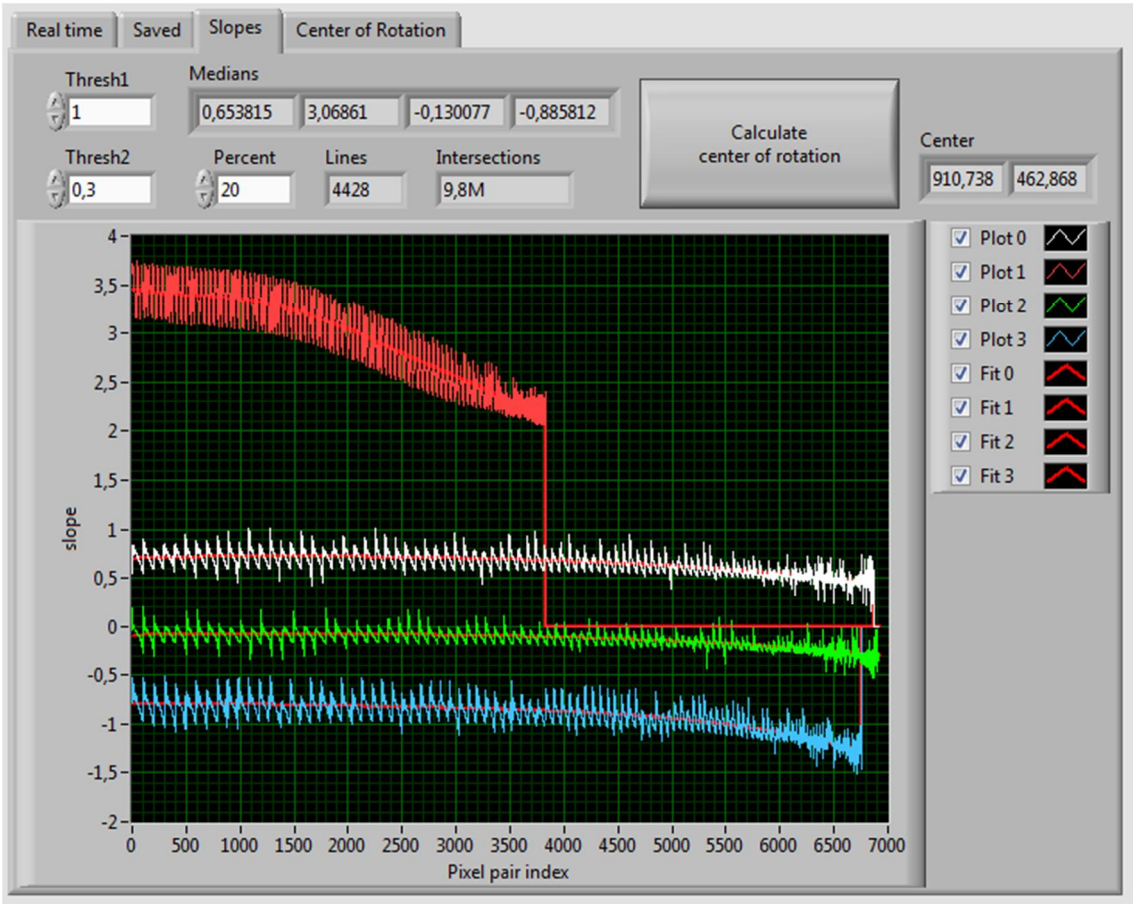


**Figure 24: LabVIEW implementation of the program.**

After filtering, the amount of accepted slope values for each corner path can vary, and the apparent value drop to zero in Figure 24 is simply a graphical consequence of how graphs of varying length are drawn on a same image on LabVIEW. This has no effect on calculations.

When the coordinates of the center of rotation have been calculated, the program is used to display sample position relative to the center of rotation in real time. This information is then used by the operator to align the sample in such a way that the distances go to zero.

## 3.4. **Perspective error**

If the top camera is not exactly centered at the turntable's vertical axis of rotation, all circles will be projected as ellipses in the image plane. Eccentricity is a function which describes the flatness of an ellipse. It is calculated from the ratio between ellipse's semi-major axis a and semi-minor axis b, shown in equation (3.6),

$$\varepsilon = \sqrt{1 - \left(\frac{b}{a}\right)^2}. \tag{3.6}$$

Eccentricity is a number between zero and one, where a zero denotes a perfect circle. Although the eccentricity of an ellipse is simply the ratio of its axes, and absolute dimensions are not needed for eccentricity alone, camera height $h$ and circle radius $R$ are needed to tie the camera zenith angle $\theta$ and perceived eccentricity together in equation (3.7),

$$\varepsilon = \sqrt{1 - \left(\frac{h}{2R}(\tan\beta_a + \tan\beta_b)\right)^2}, \tag{3.7}$$

where $\beta_a$ and $\beta_b$ are auxiliary variables defined in equations (3.8) and (3.9),

$$\cos\beta_a = \frac{1}{2h} + \frac{h^2 - R^2}{2h\sqrt{R^2 + h^2 - 2Rh\cos\left(\frac{\pi}{2} + \theta\right)}} \tag{3.8}$$

$$\cos\beta_b = \frac{1}{2h} + \frac{h^2 - R^2}{2h\sqrt{R^2 + h^2 - 2Rh\cos\left(\frac{\pi}{2} - \theta\right)}}. \tag{3.9}$$

Combining equations (3.7), (3.8) and (3.9) shows us that the perceived eccentricity of the circle is a function of circle radius $R$, camera height $h$, and camera zenith angle $\theta$. By using values R = 15 cm h = 80 cm, the eccentricity follows the curve shown in Figure 25.

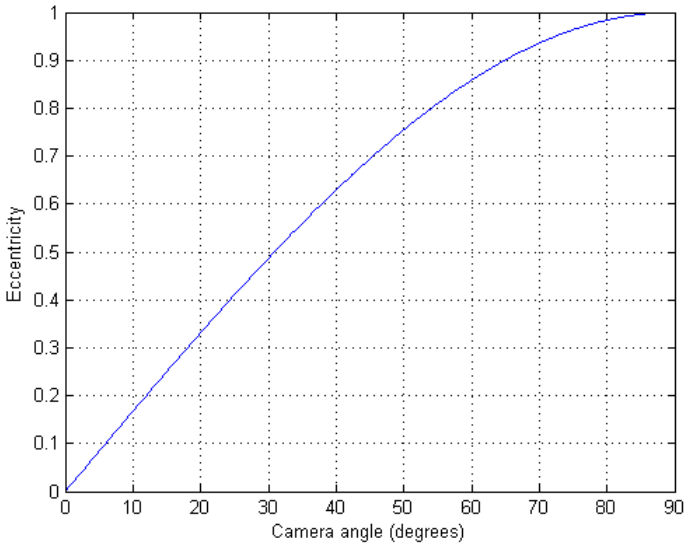


**Figure 25: Relation between the camera zenith angle and perceived eccentricity at the camera height of 80 cm and circle radius 15 cm.**

As discussed in section 3.3, the algorithm uses bisector data to calculate the center of rotation. Tangents drawn to equivalent positions at the circumference of a circle and an ellipse do not share the same slope values, and neither do their normal vectors. The ratio of normal slopes of ellipse $k_e$, and circle $k_c$, are shown in Appendix A to only be dependent on the eccentricity of the perceived circle according to equation (3.10),

$$\frac{k_e}{k_c} = \frac{1}{\sqrt{1-\varepsilon^2}}. \tag{3.10}$$

The amount of error this causes on the slope values is indicated in Figure 26.

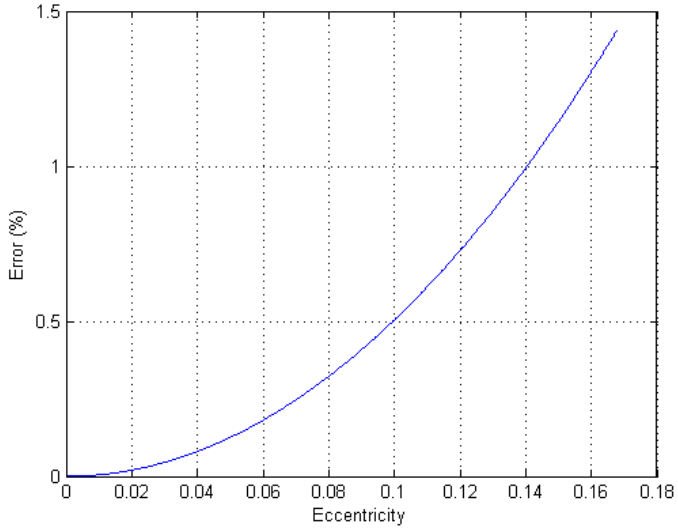


**Figure 26: Bisector slope error as a function of perceived eccentricity.**

There are two ways to mitigate perspective error. The first is to use the top camera to examine and minimize the perceived eccentricity of the turntable, which is known to have a circular edge. The second error mitigation method arises from the observation that the direction of perspective error is always such that the intersections of ellipse normal vectors will drift away from the ellipse center along its semi-major axis. Therefore the significance of this error can be reduced by roughly placing the sample as close to the center as possible when performing the alignment algorithm. This ensures that the error from one side of the image is mostly negated by an equal error from the opposite side of the image.

# 4. Measurements

The purpose of the measurements was to study the effects of different sources of uncertainty, and to show that a reasonable accuracy could be achieved even with modest equipment.

## 4.1. **Side camera**

The camera placed on the side of the device is used to detect straight lines from the sample and a vertically placed metal pole, which acts as a fixed reference. The reference pole is assumed to be at 0 degree angle, so when the edge of the pole is measured by the camera, we are measuring the angle at which the camera is in. This angle was measured in three different lighting conditions to establish the accuracy of the camera in this setup. Different lighting conditions tested were normal office lighting by ceiling fluorescent lamps, dark room without lights, and dark room with LED front lighting. The camera view of the reference pole is shown in Figure 27.

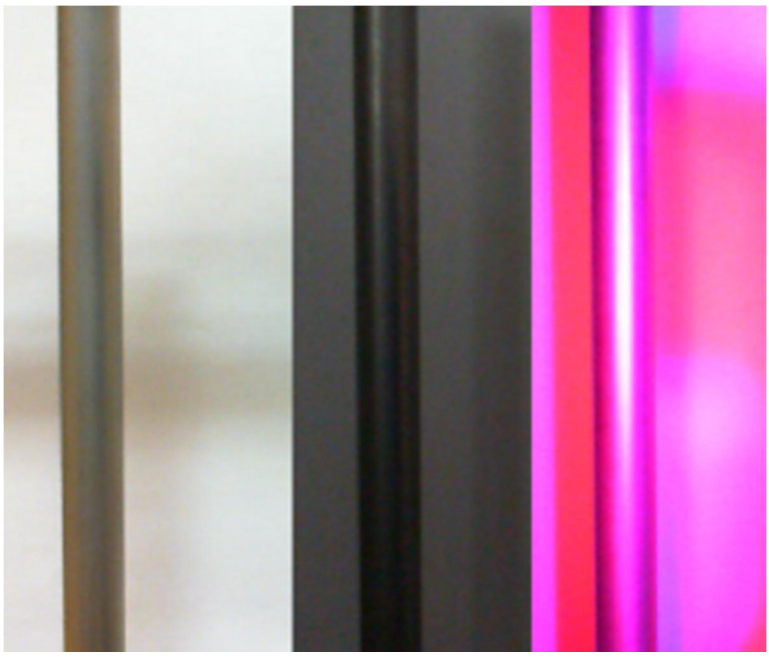

(a) (b) (c)

**Figure 27: Camera view of the reference pole at 20 cm distance in a) fluorescent lighting, b) dark room and c) with LED front lighting. Width of the reference pole is roughly 1.2 cm.**

In each scenario, the edge detection algorithm was used on the left side of the pole. The results are shown in Figure 28. Each data point represents a mean value of detected edge angle from 150 images, or frames of video. The error bars describe the standard deviations of the specific set of 150 frames.

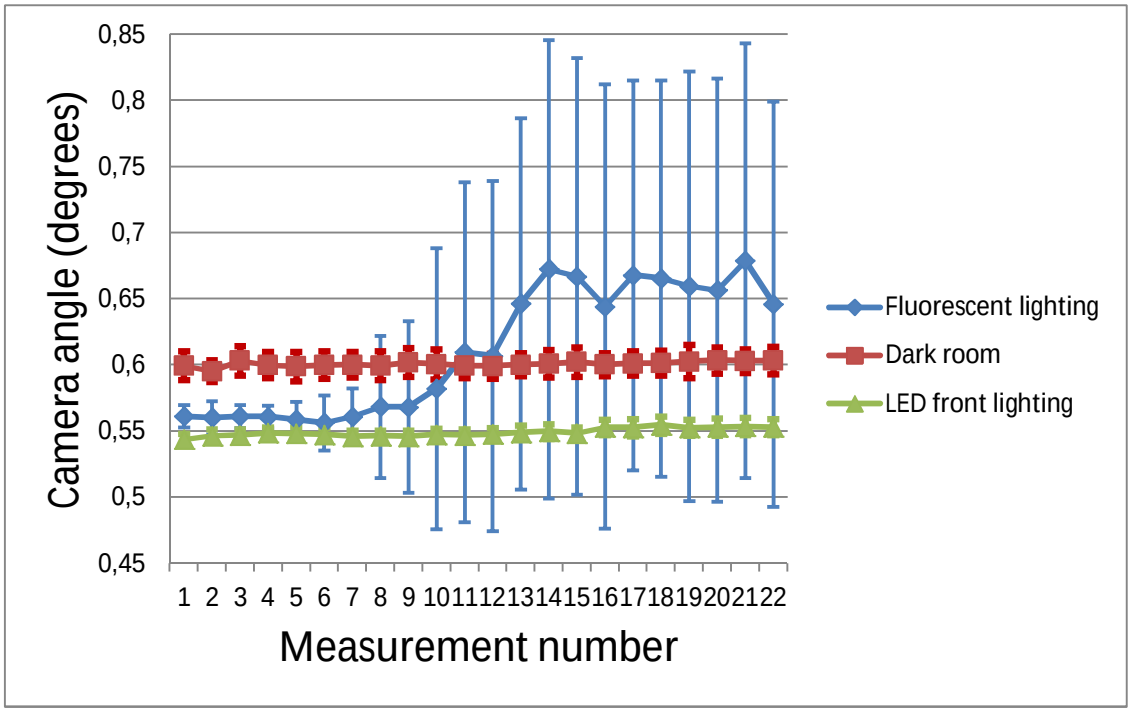


**Figure 28: Detected camera angle in various lighting conditions.**

In the case of fluorescent lighting, there was a feature in the camera which speeded up the frame rate of the video to 30 fps due to good lighting conditions. The frame rate on the two other conditions stayed considerably lower. When a digital camera is taking a picture, incoming light is converted into an electrical charge, accumulated over the time of exposure. Brighter light accumulates a higher charge, and thus image can be formed. Unfortunately, the random thermal motion of charge carriers, also known as Johnson-Nyquist noise, is unavoidable, and also affects the accumulated electrical charge. It is possible that the increased frame rate heats up the sensor, increasing thermal noise in the photosensitive diodes. This could explain the drastic increase in the uncertainty of measurements in subsequent samples with fluorescent lighting.

Dark room and LED lit scenarios both show good repeatability, since the camera is known to have fairly good low light performance, and the LED lighting creates a sharp black edge for the edge detection algorithm to work on. In the dark room scenario, ambient light coming from a window causes consistent, but uneven illumination. This leads to the algorithm to detect the edge differently at the top and bottom parts of the image, which could explain the constant difference of about 0.05 degrees between the dark and LED lit scenarios.

## 4.2. **Top camera**

The top mounted camera has two functions. Similarly to the side camera, it was used to detect changes in the rotational angle of the sample, although a reference was not defined and absolute angle was not resolved in the test setup. The second function was to resolve the turntable axis of rotation so that the sample surface could be placed on it.

### 4.2.1. Simulated setup alignment

The gonioreflectometer [1] that this system is intended to be used with contains a large, clearly visible turntable, which can be used in accurately aligning the top camera. In the prototype, the turntable is smaller, and therefore the alignment accuracy based on eccentricity was tested on a simulated setup, shown in Figure 29.

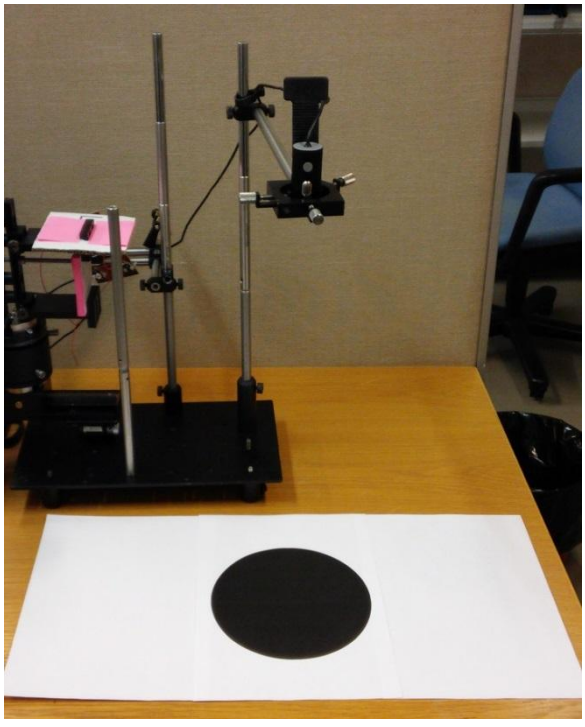

**Figure 29: Test setup for measuring perceived eccentricity of a circle.**

Even without accurate linear translators, alignment with perceived eccentricity less than 0.02 was easily attainable. By equation (3.10), this amounts to slope error less than 0.02%.

### 4.2.2. Test setup alignment

The turntable to be used in the gonioreflectometer is much larger and will be used to align the top camera as shown in section 4.2.1. However, the view of the turntable is obstructed by other parts of the device on the sample alignment process prototype. The proper positioning of the top camera was therefore achieved by aligning image features to the crosshair shown in Figure 30.

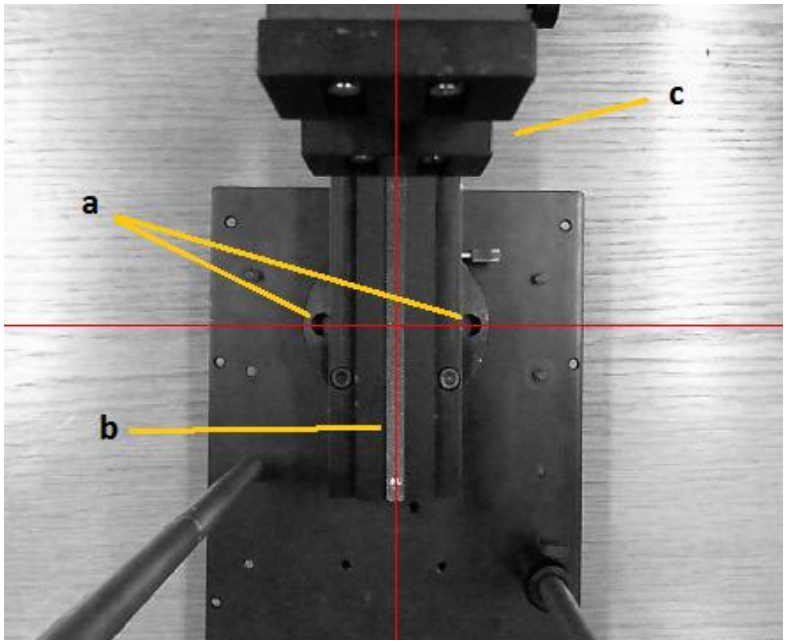


**Figure 30: Measurement prototype alignment process. Turntable holes (a), sample holder rail (b) and sample holder (c) are aligned to the red crosshair.**

### 4.2.3. Corner detection

The accuracy of corner detection was measured in two different scenarios; in a fluorescent ceiling lighting, and in a dark room. In this setup, the top camera does not have a direct view of the sample, since it's being blocked by the sample holder itself. The sample holder has clear rectangular shape, which makes it easy for the program to track the holder corners. In both scenarios, the sample holder was held in place as the camera tracked the corners for the duration of 300 frames. The results are shown in Figure 31.

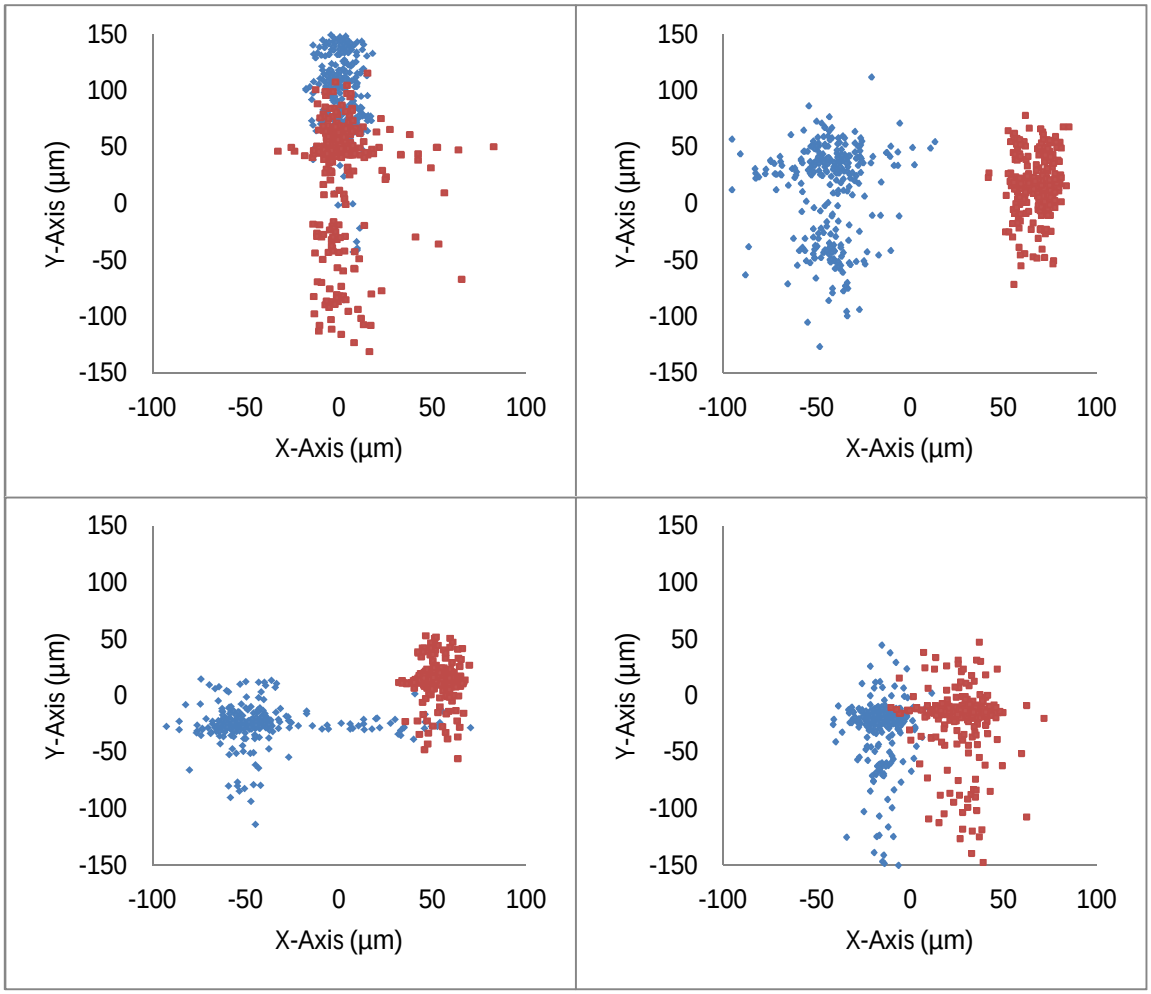


**Figure 31: Spatial accuracy of corner detection. Dark room scenario in blue, and fluorescent lighting scenario in red. LED lit scenario was not studied in the prototype due to difficulties in attaching the lights to the top camera.**

As seen from equation (3.1), the spatial resolution of the camera is dependent on the camera to sample distance, and in this case it was found to be 160µm/pixel. The average standard deviation was 0.3 pixels, or 48µm.

## 4.3. **Center of rotation**

### 4.3.1. Filtering algorithm

As mentioned in section 3.3, the number of bisector intersections can easily get unreasonably high, which is why some filtering is required. The last part of the chosen method was to randomly choose certain amount of intersections to work with. First, the movement of the sample holder was tracked as it was turned on the turntable from -10 to 10 degree position, and the sample holder corner paths were recorded, shown in

Figure 32. The resulting bisectors were calculated, and bisector filters set so that the center of rotation would be calculated from roughly 10 million bisector intersections.

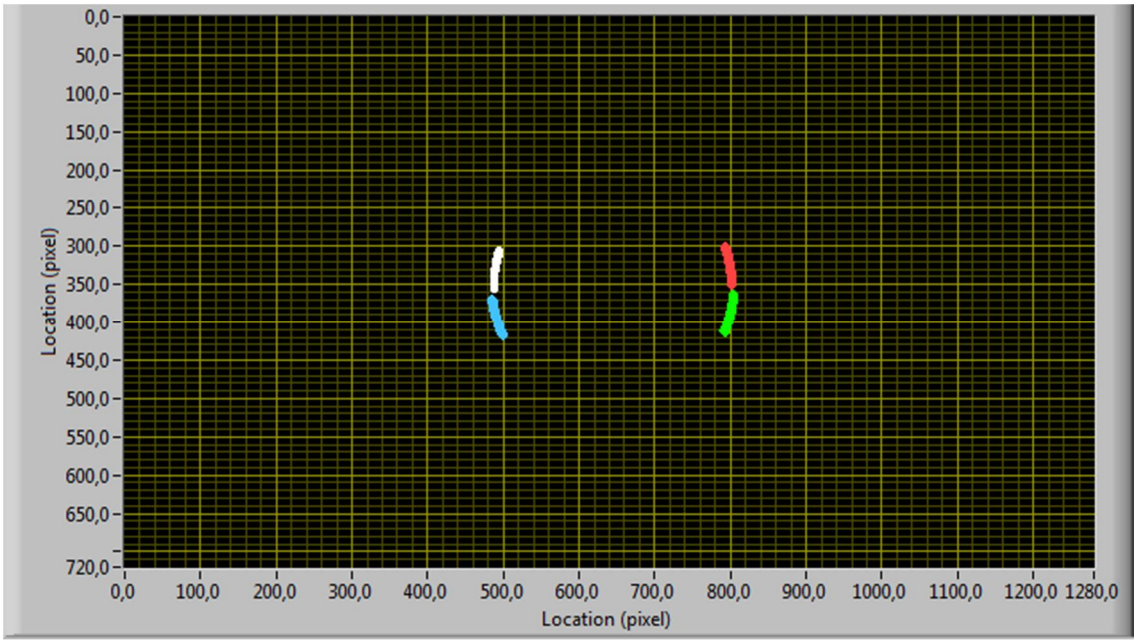


**Figure 32: Recorded corner paths in fluorescent lighting.**

Since the final filter is inherently random, its effect was studied by calculating the center of rotation multiple times from different intersection subsets of equal size. Figure 33 shows the results of this measurement, where each set of points is calculated from one data set, and each point represents a random selection within that data set.

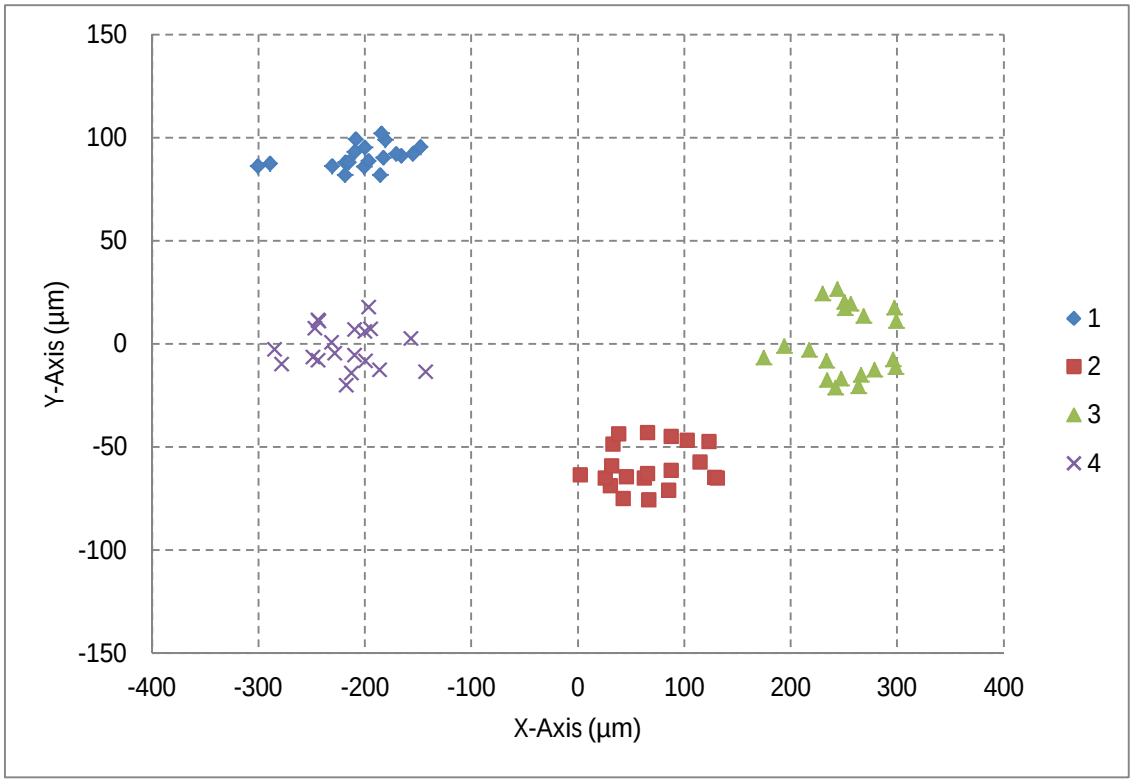


**Figure 33: Variation in the center of rotation determination in separate measurements.**

Note that the spacing on the horizontal axis is much larger than on the vertical axis. This shows one limitation of the detection algorithm. The system had trouble detecting the sample holder correctly if it was rotated much more than 10 degrees. This means that in the scenario shown in Figure 32, where bisectors are almost parallel to the horizontal axis, any error in bisector slope values will affect more on the horizontal axis than vertical. The combined uncertainty for a given set was 0.22 and 0.06 pixels, or 36 µm and 10 µm for X- and Y-axis, respectively. The variation between different sets is studied in section 4.3.2 below.

### 4.3.2. Uncertainty of alignment algorithm

Every time the sample holder is rotated, the exact path recorded will have variations. This is already seen in Figure 33, where each grouping of points was distinctly separated from each other. The effect of this variation was studied further by performing the entire alignment process multiple times. The results are shown in Figure 34.

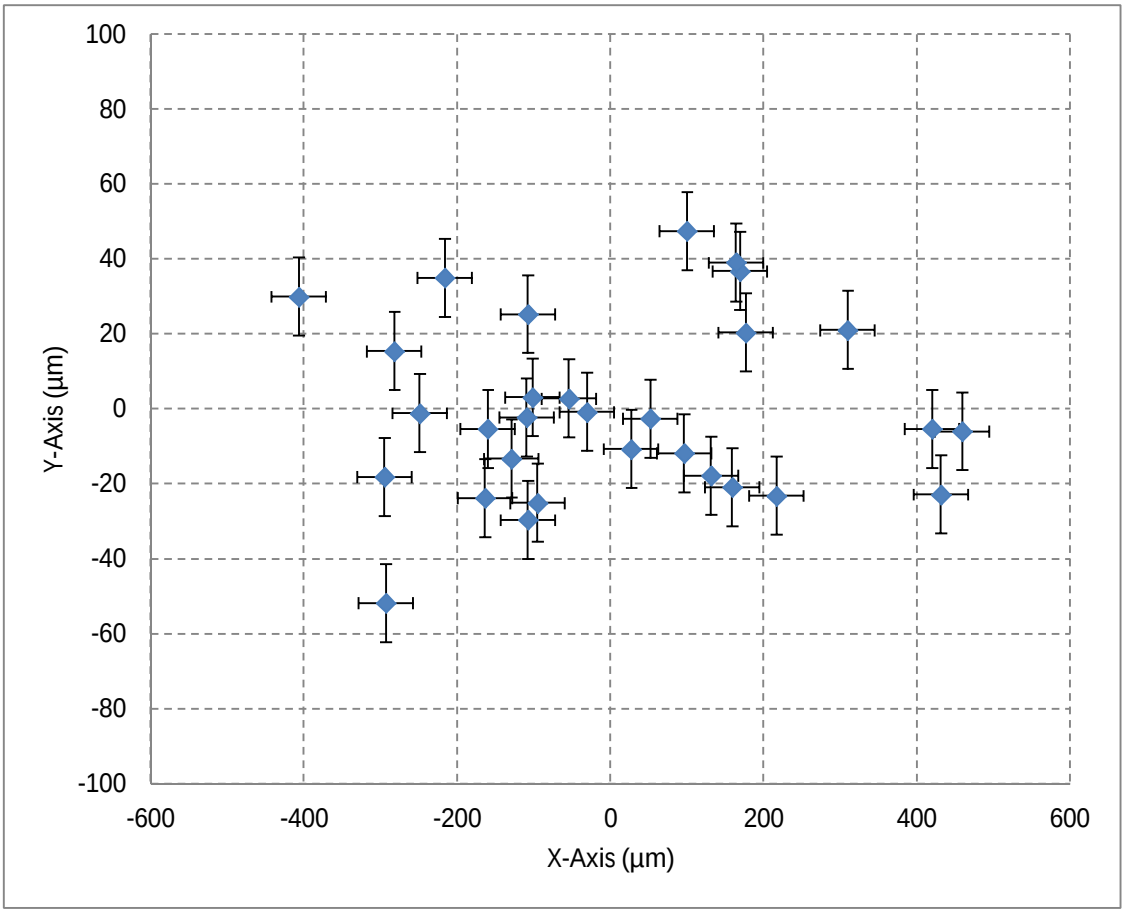


**Figure 34: Uncertainty of alignment algorithm**

As a whole, the standard deviation of the alignment algorithm was found to be 1.39 and 0.14 pixels, or 230 µm and 23 µm for X- and Y-axis, respectively. Since the standard deviations of these results are larger than for the points they are calculated from, discussed in section 4.2.3, it is likely that the largest contributor to the uncertainty of alignment is the stability of the sample holder.

# 5. Summary and conclusions

The purpose of this work was to design a method for resolving sample position and alignment as a part of a diffuse reflectance measurement device known as the gonioreflectometer. Many currently existing implementations utilize a separate specularly reflecting alignment sample, which in conjunction with a laser beam and a detector can be used to align the sample to great accuracy. Since we are interested in the measurement of diffusely reflecting surfaces, having to use a separate alignment piece is inconvenient, and changing the sample after the alignment exposes the system to an error that can't be measured.

The method chosen was to use fixed cameras to track moving features in the measurement setup. One camera placed at the side of the sample was used to detect sample edge as a straight line, from which the zenith angle of the sample can be resolved. The second camera was placed directly on top of the sample. This camera can similarly detect the rotational angle of the sample, but it also had a second purpose. In a gonioreflectometer, the sample is placed on a turntable, and to preserve the geometry of the setup during measurements, the sample has to be placed accurately at the center of the turntable. An algorithm was designed, where the center of rotation could be resolved by tracking the movement of the sample as it was rotated. After the coordinates for the center of rotation have been resolved, the sample surface could simply be placed at those coordinates.

A prototype setup was built to study the uncertainties and sources of error that affect the camera based alignment setup. Four main sources of error were identified. First one is lighting conditions. Since all features of the setup are detected from images captured by the camera, the features to be captured should be made as distinct as possible. In section 4.1, the accuracy of sample angle was studied in different lighting conditions, and a systematic difference of 0.05 degrees was observed between dark room and LED lit scenarios. The likely reason for this is that uneven illumination can cause parts of the scene to appear differently on the image, which affects the accuracy of the detection algorithm. Lighting also causes shadows, and sharp shadows in the image will make it harder for the program to distinguish between object edge and shadow edge. Shadows can be diminished by investing in good light sources and large diffusors, although the space requirements for best systems may be prohibitive in a typical laboratory.

The second source of error is the alignment of the camera itself. The side camera is more tolerant in that regard, since a vertical reference can be easily created for example with a metal pole or a suspended weight. For the top camera though, the placement is more crucial. The algorithm which detects the center of rotation relies on a detection of an arc of a circle, and if the camera is not placed at the turntable axis of rotation, circles will be seen as ellipses by the camera. The position of the camera could be resolved by examining the eccentricity of known circles apparent in the gonioreflectometer. The accuracy of camera placement was found to be limited by the ability to finely adjust the

position of the camera; a good mounting solution utilizing linear translators is therefore recommended.

Third source of error is the detection algorithm used in the software. First portion of the algorithm is to detect features in the image. For the top camera, a rectangle detection method in LabVIEW was used. With average standard deviation of 0.3 pixels, the precision of the system was fairly good, although the accuracy remains unclear. Good knowledge of machine vision and object tracking would be very helpful in improving the detection algorithm. Second portion of the algorithm was to use a recorded feature path to calculate the center of rotation. The amount of data points that could be recorded is enormous, and as discussed in section 3.3, certain part of it is clearly erroneous, and filtering was needed. The filtering method used resulted in standard deviation of roughly 0.22 pixels. While this precision is good, it could likely be improved further with a more intelligent filtering method.

Final source of error is the equipment and the setup dimensions. While the web cameras used proved to be quite effective, better systems certainly exist. Higher resolution cameras help, but since the algorithms can already detect features with sub-pixel accuracy, low image noise is the most important factor of a camera. The camera itself can only detect per pixel, and therefore the spatial accuracy of the system will always depend on the optics and camera-to-feature distance. Best accuracy can be obtained when suitable optics is used to ensure the examined feature fills the frame as much as possible.

Overall, the introduced method for sample alignment shows promising performance. Utilizing modest equipment, angular alignment of the sample was measured to 0.01 degree accuracy and the center of rotation was resolved to 200 µm accuracy. While the accuracy of the alignment system is dependent on the geometry of the setup, the largest contributor to the uncertainty was found to be the stability of the sample holder. However, the gonioreflectometer for which this method was designed is more rigid than the prototype used in this work, and it’s likely that the largest source of error for that setup comes from the reliability of the feature detection algorithm. The method itself is effective, versatile and easy to implement. In this work, corners of a rectangle on the sample holder were observed, but the nature of a rotating disc is that any feature can be used in resolving the center of rotation.

# 6. References


[1] S Nevas, F Manoocheri, and E Ikonen, "Gonioreflectometer for measuring spectral diffuse reflectance," *Applied Optics*, vol. 43, pp. 6391-6399, 2004.

[2] G Eilertsen, P Larsson, and J Unger, "A versatile material reflectance measurement system for use in production," in *Proceedings of SIGRAD 2011. Evaluations of Graphics and Visualization*, Stockholm, 2011, pp. 69-76.

[3] D Hünerhoff, U Grusemann, and A Höpe, "A new robot-based gonioreflectometer for measuring spectral diffuse reflection," *Metrologia*, vol. 43, pp. S11-S16, 2006.

[4] J Campos et al., "Techniques for calibration of illumination/observation geometry with uncertainty of ±0.1° developed," Task 3.1: Tools and techniques for calibration of geometrical parameters of gonio-photometers and fluorometers, IND52 xDReflect project, Deliverable 3.1.1., 2014.

[5] M Curkovic and D Vucina, "3D shape acquisition and integral compact representation using optical scanning and enhanced shape parameterization," *Advanced Engineering Informatics*, vol. 28, pp. 111-126, 2014.

[6] R Minguez, A Arias, O Etxaniz, E Solaberrieta, and L Barrenetxea, "Framework for verification of positional tolerances with a 3D non-contact measurement method," *International Journal on Interactive Design and Manufacturing (IJIDeM)*, vol. in press, 2014.

[7] R Maini and H Aggarwal, "Study and Comparison of Various Image Edge Detection Techniques," *International Journal of Image Processing*, vol. 3, pp. 1-11, 2009.

[8] J Canny, "A Computational Approach to Edge Detection," *IEEE transactions on Pattern Analysis and Machine Intelligence*, vol. PAMI-8, pp. 679-698, 1986.

[9] G Hamarneh, K Althoff, and R Abu-Garbieh, "Automatic Line Detection," Chalmers University of Technology, Project report for Computer Vision Course 1999.

[10] P Sinha, *Image Acquisition and Preprocessing for Machine Vision Systems*.: SPIE Press, 2012, ch. 4.

# Appendix A

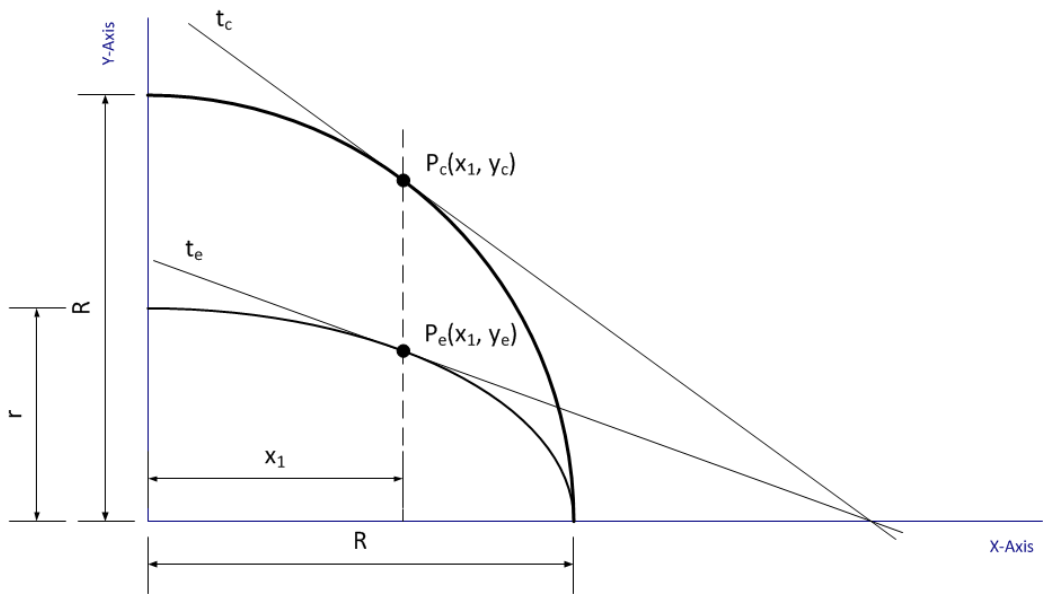


**Figure A 1: Tangents of a circle and an ellipse.**

This Appendix derives equation (3.10) of the main text. Equations for the tangent of a circle $t_c$, and the tangent of an ellipse $t_e$ are shown in equation A1,

$$\begin{aligned} t_c &\equiv x_1 x + y_c y = R^2 \\ t_e &\equiv r^2 x_1 x + R^2 y_e y = R^2 r^2. \end{aligned} \tag{A1}$$

Next, we rearrange the line equations in equation A1 to another common form, shown in equation A2,

$$\begin{aligned} y &= -\left(\frac{x_1}{y_c}\right) x + \frac{R^2}{y_c} \\ y &= -\left(\frac{r}{R}\right)^2 \left(\frac{x_1}{y_e}\right) x + \frac{r^2}{y_e}. \end{aligned} \tag{A2}$$

This makes it easy to see the values of tangent slopes $k_{ct}$ and $k_{et}$,

$$\begin{aligned} k_{ct} &= -\frac{x_1}{y_c} \\ k_{et} &= -\left(\frac{r}{R}\right)^2 \left(\frac{x_1}{y_e}\right). \end{aligned} \tag{A3}$$

Slope of a normal to a line is the negative inverse to the original line's slope,

$$k_c = -\frac{1}{k_{ct}} = \frac{y_c}{x_1}$$
$$k_e = -\frac{1}{k_{et}} = \left(\frac{R}{r}\right)^2 \left(\frac{y_e}{x_1}\right). \quad \text{A4}$$

Eccentricity of an ellipse is a function of its semi-major and semi-minor axis, where the semi-major axis in this scenario, is also the radius of the circle,

$$\varepsilon = \sqrt{1 - \left(\frac{r}{R}\right)^2}. \quad \text{A5}$$

Tangents drawn as in Figure A 1 have a relationship between their Y-coordinates,

$$y_c = \frac{R}{r} y_e. \quad \text{A6}$$

Combining equations A4-A6, we finally obtain the equations for the circle and ellipse normal slopes $k_c$ and $k_e$, shown in equation A7,

$$k_c = \left(\frac{R}{r}\right)\left(\frac{y_e}{x_1}\right) = \frac{1}{\sqrt{1-\varepsilon^2}}\left(\frac{y_e}{x_1}\right)$$
$$k_e = \left(\frac{R}{r}\right)^2\left(\frac{y_e}{x_1}\right) = \frac{1}{1-\varepsilon^2}\left(\frac{y_e}{x_1}\right). \quad \text{A7}$$

Finally, we obtain the ratio of slopes in equation A8,

$$\frac{k_e}{k_c} = \frac{1}{\sqrt{1-\varepsilon^2}}. \quad \text{A8}$$